

Article

Stabilizing effect of amino acids on protein and colloidal dispersions

<https://doi.org/10.1038/s41586-025-09506-w>

Received: 17 April 2024

Accepted: 7 August 2025

Published online: 10 September 2025

Open access

 Check for updates

Ting Mao^{1,7}, Xufeng Xu^{1,7}, Pamina M. Winkler^{1,7}, Cécilia Siri^{1,7}, Ekaterina Poliukhina¹, Paulo Jacob Silva¹, Nan Xu², Yu Hu², Karim Al Zahabi³, Rémi La Polla¹, Zhi Luo²✉, Quy Ong¹✉, Alfredo Alexander-Katz⁴✉ & Francesco Stellacci^{1,5,6}✉

Amino acids (AAs) have a long history of being used as stabilizers for biological media¹. For example, they are important components in biomedical formulations. The effect of AAs on biological systems is also starting to be appreciated. For example, it is believed that water-stressed cells increase the levels of AAs to prevent protein aggregation². Several hypotheses have been put forward regarding their function, ranging from water-structuring³ to hydrotropic⁴ to specific effects such as stabilization against misfolding, yet it is not known whether their stabilizing function is protein specific or a generic colloidal property. Here we deduce that AAs possess a new and broad colloidal property: they stabilize patchy nanoscale colloids by adsorbing onto their surfaces through weak interactions. We demonstrate this general property by careful experimental evaluation of the stabilizing effect of AAs on dispersions of various proteins, plasmid DNA and non-biological nanoparticles. Furthermore, we develop a theoretical framework that captures this phenomenon and experimentally corroborate several new broad theoretical implications that apply beyond AAs. In vivo experiments further demonstrate that the addition of 1 M proline to insulin doubles its bioavailability in blood. Overall, our results indicate that the role of small molecules is as important as that of ionic strength and should always be reported in biophysics experiments.

Colloidal interactions, from weak to strong, are a key component of non-biological as well as biological processes (for example, protein–protein interactions, PPIs). Controlling and regulating these interactions is at the core of formulation development. In terms of medical formulations, controlling PPIs is key to preventing protein degradation and aggregation, which in turn is believed to increase bioavailability. For many decades, amino acids (AAs) have been widely used to stabilize biological formulations, yet despite such widespread use, we are far from understanding the nature of the stabilizing effect of AAs on dispersions. We do not even know if it is a specific biological effect as opposed to being a generic colloidal property. There have been many proposed mechanisms to explain these broad stabilization properties. Most of the literature points towards the effect of AAs in stabilizing the folded state⁵, yet there have been other hypotheses that consider them as molecular lubricants for proteins (hydrotropes)⁴. Other mechanisms involve AA strong effects on the water H-bonding structure³. In biological systems, the role of AAs in the cytosol of cells has been a topic of investigation for years. It was reported that almost all water-stressed organisms reduce the aggregation of proteins in cells by raising the concentration of AAs such as proline and glutamic acid⁶. For example, *Escherichia coli* regulates cytosolic proline concentration to inhibit the initial aggregation process of cellular retinoic acid-binding proteins⁷.

To the best of our knowledge, however, no study exists on the effect of AAs in stabilizing dispersions of non-biological colloids, and most explanations of their role consistently imply some form of biological effect. Furthermore, we are not aware of any predictive theory that would be able, from an independent measurement, to derive whether a specific AA or an additive can stabilize a given protein.

Here we study the effect of AAs on a wide range of colloidal dispersions (proteins, nanoparticles and plasmid DNA) by measuring the second osmotic virial coefficient (B_{22}) as well as the potential of mean force (PMF). An increase in B_{22} implies a more stable dispersion because it indicates a stronger repulsion among colloids. Conversely, a decrease in B_{22} indicates that attractive forces are becoming more dominant and may lead to destabilization of the dispersion. Adding salt typically destabilizes suspensions, as measured by a decrease in B_{22} . However, in all cases, when we added AAs to dispersions of nanoscale colloids, we found an increase in B_{22} , indicating more stable dispersions. Changes in B_{22} were detected at concentrations as low as 10 mM with no concentration threshold and at protein to AAs stoichiometric ratios as low as 1:7. We postulate that the effect is due to weak AA–colloid interactions that in turn modulate the colloid–colloid self-interactions. On the basis of this hypothesis, we develop a theoretical framework that considers proteins (or more generally colloids) as patchy particles, and the number

¹Institute of Materials, Ecole Polytechnique Fédérale de Lausanne, Lausanne, Switzerland. ²Department of Biomedical Engineering, Southern University of Science and Technology, Shenzhen, People's Republic of China. ³Department of Chemical Engineering, Massachusetts Institute of Technology, Cambridge, MA, USA. ⁴Department of Materials Science and Engineering, Massachusetts Institute of Technology, Cambridge, MA, USA. ⁵Bioengineering Institute, Ecole Polytechnique Fédérale de Lausanne, Lausanne, Switzerland. ⁶Global Health Institute, Ecole Polytechnique Fédérale de Lausanne, Lausanne, Switzerland. ⁷These authors contributed equally: Ting Mao, Xufeng Xu, Pamina M. Winkler, Cécilia Siri. ✉e-mail: luoz@sustech.edu.cn; quy.ong@epfl.ch; aalexand@MIT.EDU; francesco.stellacci@epfl.ch

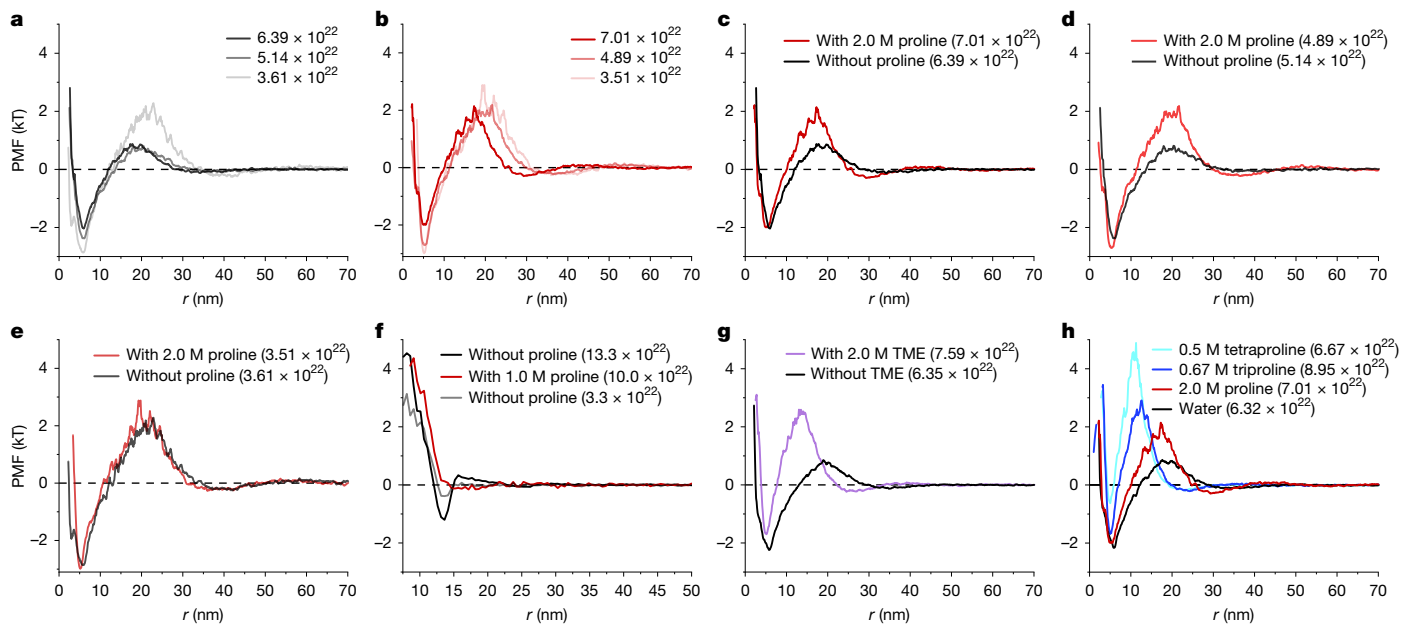


Fig. 1 | PMFs of Au nanoparticles and ferritin in different solvent additives and concentrations. **a**, PMF of AuNPs dispersion in water for different particle concentrations. **b**, PMF of the same AuNPs dispersions in 2.0 M proline for different particle concentrations. **c–e**, The proline effect (red) in comparison with pure water (black) of the AuNPs of a similar number concentration. **f**, PMF of ferritin in 50 mM phosphate buffer, as well as with the addition of 1.0 M proline. **g**, PMF of AuNPs in water in contrast with the addition of 2.0 M TME. **h**, PMF of Au nanoparticles in water (solid black), 2.0 M proline (red), 0.67 M triproline (blue) and 0.5 M tetraproline (cyan). In case of the PMFs shown in **g** and **h**, we should note that the barrier position moves to shorter distances and its height increases consistently with the effect of the molecules added that stabilize the monomeric form of the nanoparticles against their aggregated one. The numbers in the legends indicate the number concentration of the particle in particles m^{-3} .

1,1,1-tris(hydroxymethyl)ethane (TME). **h**, PMF of Au nanoparticles in water (solid black), 2.0 M proline (red), 0.67 M triproline (blue) and 0.5 M tetraproline (cyan). In case of the PMFs shown in **g** and **h**, we should note that the barrier position moves to shorter distances and its height increases consistently with the effect of the molecules added that stabilize the monomeric form of the nanoparticles against their aggregated one. The numbers in the legends indicate the number concentration of the particle in particles m^{-3} .

of effective patches is determined by how many of these sites are not blocked by bound AAs. The number of blocked patches is assumed to follow a Langmuir isotherm, whereas the stability of the colloids is evaluated at the mean-field level. Results from this theory have the following implications: (1) charged AAs will be effective only for proteins of opposite charge; (2) short peptides composed of n AAs will be as or more effective than n separate AAs; (3) any small molecule weakly interacting with nanoscale colloids will stabilize them through the same effect. Experiments corroborate all three predictions. Importantly, we find excellent quantitative agreement between the equilibrium dissociation constants for AA/proteins obtained by direct measurements as compared with those found by fitting the experimental data with this theory (for example, proline/lysozyme 1.12 M and 2.28 M, respectively). Our theoretical framework provides a new way to understand the stabilizing role of AAs as well as other small molecules on colloidal dispersions.

Stabilization of colloidal dispersions by AAs

To investigate whether the ability of AAs to stabilize protein dispersions is a colloidal or a protein-specific property, we explored the effect of proline on gold nanoparticles (AuNPs) coated with a mixture of hydrophobic and hydrophilic ligands. The latter are nanoscale colloids that have marked differences when compared with proteins. For example, no misfolding is possible in AuNPs. Specifically, we used AuNPs with a diameter of 3.5 nm coated with $(56.5 \pm 4.3)\%$ of mercapto-undecane sodium sulfonate and $(43.5 \pm 4.3)\%$ of octanethiol (true stoichiometric ratio, see Supplementary Fig. 1 for the experimental determination). The nanoparticles in water form a stable suspension, as determined by experiments performed in analytical ultracentrifugation–sedimentation equilibrium (AUC-SE)⁸, showing angular-velocity-dependent equation of state (EOS) curves⁹ (Supplementary Fig. 2). We used a recently developed cryo-electron microscopy method¹⁰ to derive the PMF of the particles. In Fig. 1a, we show

PMF curves in water at varying particle concentrations. In all three curves, there is a minimum in the potential at about 7 nm because of the formation of aggregates; at about 20 nm, we find the corresponding energy barrier, the cause of which is discussed in the Methods. The attractive potential for these particles consists of two parts: a hydrophobic short-range (< 3 nm) component plus a longer-range electrostatic attraction due to plasmon coupling. This interpretation of the curves is consistent with recent literature¹¹. The minimum in the potential depends on the concentration of the particles in its magnitude, becoming slightly deeper as the concentration decreases, but its position stays constant. The barrier height becomes smaller and the barrier position moves to shorter distances as the concentration of the particles increases. This decrease in the barrier with an increase in concentration can be explained because of the polarization of the gold cores, which will significantly reduce the electrostatic energy of two particles coming together. The energy difference between the potential minimum and the barrier height is of the order of 3–4 kT, which suggests the aggregation is dynamic in these suspensions. For comparison, in Fig. 1b, we present the PMF for the same nanoparticles in a solution containing proline at a concentration of 2.0 M. As we vary nanoparticle concentrations, the minimum of the potential shows the same behaviour as observed in the absence of proline. By contrast, however, the concentration dependence of the energy barrier is very different when proline is present. In this case, the barrier height is independent of the nanoparticle concentration, and its position varies only minimally with it. In Fig. 1c–e, we present the same data shown in Fig. 1a,b in a different way, namely, we compare directly suspensions at the same nanoparticle concentration with and without proline. It is immediately evident that proline has no clear effect on the minimum of the potential, but it increases the barrier height. As expected, the effect diminishes with decreasing concentration as the suspensions behave closer to their ideal limit. We used the same approach to investigate the effect of proline on ferritin, a protein that is simple to image in cryo-EM. As shown in Fig. 1f, the PMF for ferritin

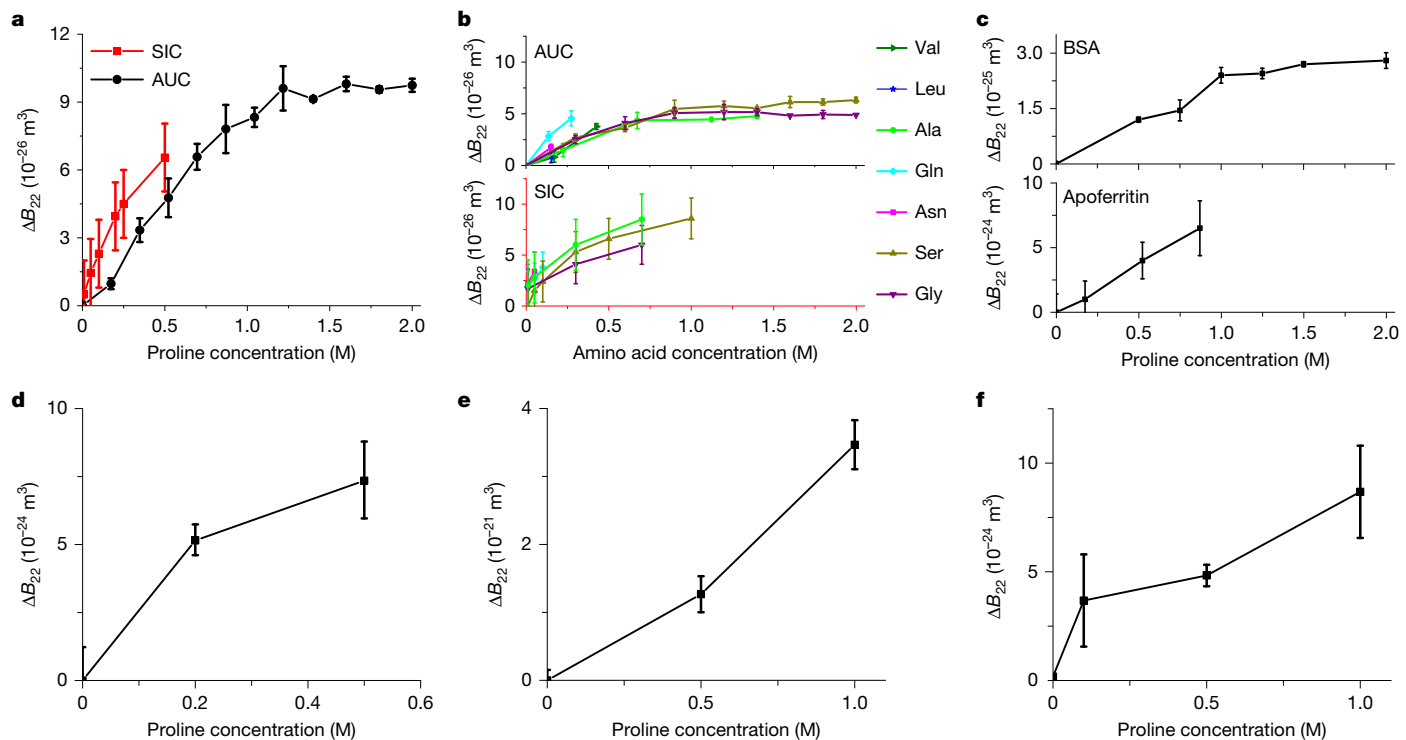


Fig. 2 | Change of the second virial coefficient B_{22} (ΔB_{22}) for different self-interactions as a function of added AAs. **a,b**, By applying sedimentation diffusion equilibrium analytical ultracentrifugation (SE-AUC, in black) and self-interaction chromatography (SIC, in red), we quantify the influence of increasing proline concentration (a) and different AAs (b) on the self-interaction of lysozyme. **c–f**, By applying SE-AUC, we measure the modulation on the addition of proline on the self-interacting BSA and apoferritin (c),

FUS-LCD (d), DNA (e) and Au NPs (f). Note that SIC has been established with lysozyme being manually grafted to the column; thus, only the self-interaction of lysozyme can be probed. To prevent the clogging of the SIC column, the effect of small molecules is typically investigated in the concentration range below 1.0 M, especially for less soluble molecules. Data are presented as mean \pm 1 s.d.; $n = 3$ independent experiments.

also shows a minimum and a small aggregation barrier and the addition of 1.0 M proline renders the PMF much closer to that of ferritin at a lower concentration. Overall, this set of data indicates that proline stabilizes colloidal suspensions as its addition renders the PMFs closer to those of suspensions at lower concentrations. More importantly, we find that the proline effect seems to be very similar in the case of a protein and a nanoparticle, suggesting a colloidal effect and not a protein-specific one.

We used AUC-SE¹² and self-interaction chromatography (SIC)¹³ to measure B_{22} (Methods). Changes in B_{22} reveal the relative attractive or repulsive components of an effective inter-colloidal potential. The choice of two independent methods based on different physical principles was made to avoid any possible measurement-related bias or error¹⁴. We measured the change of B_{22} (ΔB_{22}) as a function of the concentration of AAs in dispersion. A positive change ($\Delta B_{22} > 0$) indicates that, in the dispersion, the net interactions become more repulsive (that is, the difference between repulsion and attraction grows in favour of the former). As expected, we find that adding salt or a suitable polymer to a protein dispersion leads to a $\Delta B_{22} < 0$ because of increased electrostatic screening or depletion forces, respectively (Supplementary Table 1). As shown in Fig. 2, the addition of proline to a dispersion of lysozyme, bovine serum albumin (BSA), apoferritin or fused in sarcoma (FUS) low-complexity domain (LCD) (residues 1–267; ref. 15) (Fig. 2a,c,d, respectively) leads to a positive change in B_{22} ($\Delta B_{22} > 0$), despite an obvious increase in the ionic strength due to the zwitterionic nature of proline at buffer pH 7.0 (isoelectric point of proline: 6.3). Similar results were observed when proline was added to a dispersion of plasmid DNA (Fig. 2e), or the nanoparticles described above (Fig. 2f). Proline was used as a representative AA, yet all AAs that we tested yielded $\Delta B_{22} > 0$ for lysozyme (Fig. 2b). It should

be stressed that there is an important difference between proteins and nanoparticles. The former can change conformation (through misfolding or smaller transient conformational changes), but the latter cannot¹⁶. The fact that $\Delta B_{22} > 0$ on AAs addition for both cases suggests that conformational changes are not the reason for this phenomenon. In a recent publication⁹, we have shown that lysozyme and BSA dispersions are solutions, whereas apoferritin is a suspension. Hence, the thermodynamic status of the dispersion seems not to be relevant for this effect to occur. Apoferritin (molecular weight $M_w = 480,000$ Da) and plasmid DNA ($M_w = 2,600,000$ Da) are much larger than lysozyme ($M_w = 14,300$ Da) and BSA ($M_w = 66,000$ Da), indicating an effect that happens over a wide span of sizes. FUS-LCD is an intrinsically disordered protein, whereas the other proteins we tested are folded ones. Yet, they all similarly change B_{22} on proline addition.

Theoretical framework and its validation

We propose a theoretical framework to explain all the experimental observations presented here. It is based on the hypothesis that weak interactions between the AAs and the colloids in dispersion lead to a time-averaged screening of colloid–colloid attractive interactions (Fig. 3). As described above, the theory considers the colloids as patchy particles and the adsorption of AAs to the surface by a Langmuir-type isotherm. Using these ingredients, we derive the following formula for the change in B_{22} as a function of AAs/small molecule concentration c (see Methods for a rigorous derivation):

$$\Delta B_{22} = (a^3 - B_{22}^0) \frac{Kc}{1 + Kc} f_{\max} \quad (1)$$

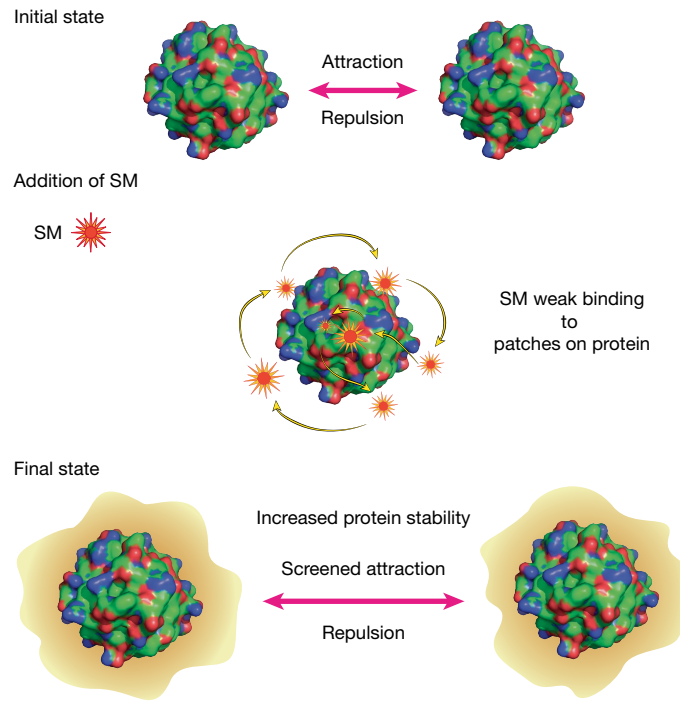


Fig. 3 | Schematic of the proposed theoretical framework for increase in colloidal stability caused by small molecules. A protein is drawn as a spherical blob decorated by patches of different charges and hydrophobicity, each of which is given an artificial colour to highlight the patchy interaction model of the protein. A small circle surrounded by multiple spikes represents graphically a small molecule. Its interaction with the protein is shown as staying close, mainly to the hydrophobic patches. Its time-averaged localization around the protein is shown as yellow arrows that evolve into a yellow halo as a time average of the local concentration around the protein, which then leads to a stronger net repulsion among proteins.

where a^3 corresponds to an effective excluded volume, B_{22}^0 is B_{22} of the colloid in the absence of the small molecule of interest, K is the equilibrium association constant and f_{\max} is the maximum surface fraction of the colloid that can be masked by the small molecules.

Using equation (1), we were able to fit all the data we presented on the change of the experimental B_{22} , ΔB_{22} , as a function of concentration c of AAs. For proline, glycine, serine and alanine, we had enough data points to achieve reliable fits. We started by fitting the proline data because they had the most data points. We did so by floating the K and a parameters while keeping f_{\max} to an arbitrary value of 1 and obtained an a^3 of $1.75 \times 10^{-25} \pm 2.2 \times 10^{-26} \text{ m}^3$ and K of $0.89 \pm 0.26 \text{ M}^{-1}$ (Table 1; for detailed fitting, see Extended Data Fig. 1). We first comment on a , whose value implies a diameter of 5.6 nm. The maximum value of B_{22} that a molecule can attain for the screening is a^3 , and it encompasses two contributions: hard-sphere exclusion volume and charge repulsion. The value a must be slightly larger than the hard-sphere diameter of lysozyme, and it is in good agreement with the hydrodynamic diameter of lysozyme that we measured with dynamic light scattering (DLS) to be 4.1 nm (Supplementary Fig. 3) also matching the reported literature value¹⁷. For the other AAs, we constrained f_{\max} to be the ratio of the plateau found in the ΔB_{22} plot of the AA to that of the plot for proline and used this to fit the data. We obtained the values for K (Table 1) and the values of a (Extended Data Fig. 1). It is immediately noticeable that the obtained values of a from the fit are only within 8% from each other. The quality of all fits is good as indicated by the value of adjusted R^2 , which is greater than 0.96 (Extended Data Fig. 1). We also measured the interaction of AAs with lysozyme experimentally by using intrinsic fluorescence experiments¹⁸ (Table 1).

Table 1 | Comparison of the equilibrium binding constant K_D obtained for lysozyme

Amino acids	Proline	Glycine	Serine	Alanine
From the fit of ΔB_{22} plot ^a				
$K (\text{M}^{-1})$	0.89 ± 0.23	3.2 ± 0.98	1.55 ± 0.31	1.77 ± 0.88
$K_D (\text{M})$	1.12 ± 0.29	0.31 ± 0.09	0.64 ± 0.01	0.56 ± 0.28
From intrinsic fluorescence measurements ^b				
n	0.96 ± 0.03	0.76 ± 0.05	0.85 ± 0.08	0.92 ± 0.03
$K_D (\text{M})$	2.28 ± 0.07	5.93 ± 0.12	4.98 ± 0.36	1.76 ± 0.04

^aEquilibrium constant of binding (K) and the calculated dissociation constant ($K_D = 1/K$) by fitting the SE-AUC data with equation (1).

^b K_D measured by intrinsic fluorescence experiments for lysozyme with four different AAs—proline, glycine, serine and alanine. The number of binding sites n has been determined using equation (18) (for more details, see the Methods) obtained by fitting the intrinsic fluorescence measurements. Measurement data are shown in Supplementary Fig. 4.

For proline–lysozyme, we measure an equilibrium dissociation constant K_D of $2.28 \pm 0.07 \text{ M}$ in great agreement with the one deduced by fitting our ΔB_{22} data, $K_D = 1/K = 1.12 \pm 0.29 \text{ M}$. We observe that the experimental data and the fitted data never differ by more than an order of magnitude (Table 1), a remarkable agreement given the uncertainties involved. Intrinsic fluorescence experiments are sensitive to changes in the tryptophan fluorescence of the protein, which can be induced by direct binding of AA or by a conformational rearrangement triggered by the AA interaction^{18,19}. There are three tryptophan residues on a lysozyme surface. This experiment does not exclude binding in far-away surface sites, but given the weak nature of the interaction, we can exclude that many more AAs will bind to lysozyme from thermodynamic considerations. We also performed the same analysis for BSA, and obtained an a^3 of $1.8 \times 10^{-24} \pm 1.0 \times 10^{-25} \text{ m}^3$. This value corresponds to a diameter of about 12 nm, which is in good agreement with about 9.8 nm obtained by DLS (Supplementary Fig. 3). The K_D that leads to the best fit of ΔB_{22} data is $2.00 \pm 0.52 \text{ M}$ (Extended Data Fig. 2). We measured proline–BSA interactions by a competitive binding assay, which gave a K_D value of $3.0 \pm 1.0 \text{ M}$, which is again in excellent agreement. We show that our model can explain existing data in literature^{20–22}, where it is shown that a series of small molecules (ethanol, butanol, glycerol, sucrose and trehalose) stabilize lysozyme, and sorbitol and sucrose stabilize the protein amylase. In Extended Data Fig. 3, we show that we can fit the published data basically with the same accuracy that we find in our data. Also, in this case, we achieved values of the parameter a that are consistent with its interpretation and with each other. Furthermore, in line with our theory, all small molecules show dissociation constants in the mM to M range.

There are many direct consequences of this theory. First, AAs with charged side chains will have a stabilizing effect only on proteins of the opposite charge, and this is confirmed by our findings (Extended Data Fig. 4a,b). Second, in a first approximation, assuming the interaction scales linearly with the number of AAs per oligomer, the theory implies that short peptides composed of n AAs should produce a ΔB_{22} on a colloidal solution that is equivalent to the ΔB_{22} produced if n AAs were added separately to the solution. There may be a limit in the length of the polypeptides above which the countereffect, for example, one caused by depletion force, takes place²³. As shown in Extended Data Fig. 4c, when we measure ΔB_{22} for peptides formed by three or four prolines, we find that the obtained values of ΔB_{22} are the same as generated by proline itself (see also SIC results; Extended Data Fig. 5). We can further confirm this by studying the PMF for gold nanoparticles when these peptides of proline are added. As shown in Fig. 1h, tetra-proline seems to be even more effective than proline in stabilizing the particle solutions. Third, the theory does not imply any special property for AAs.

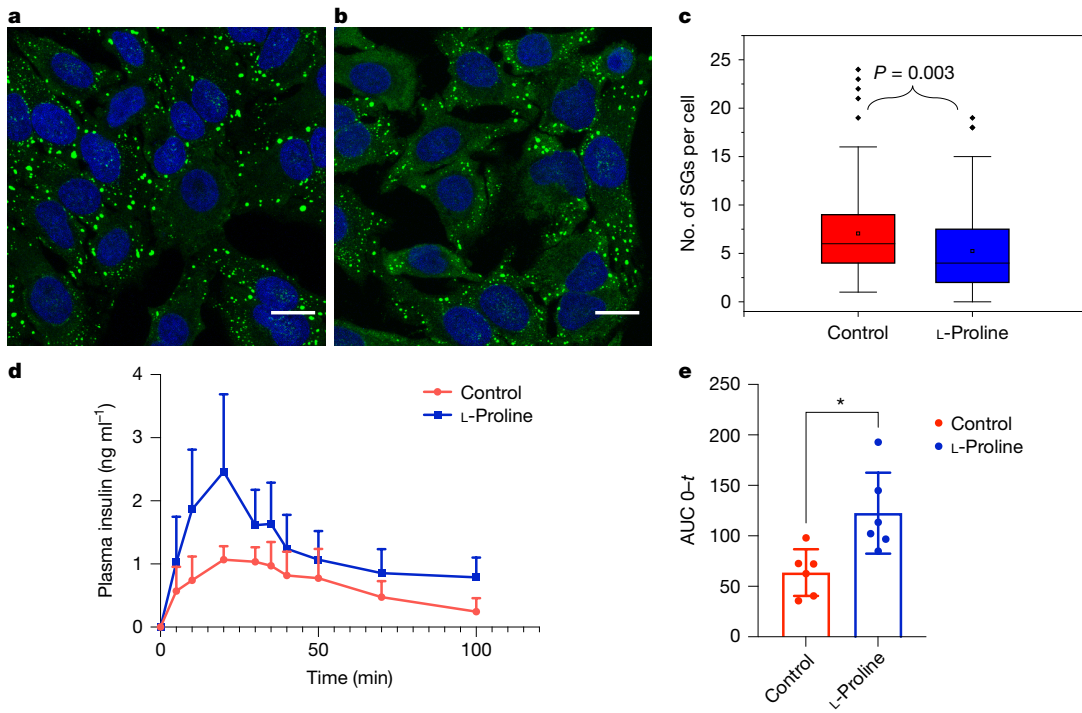


Fig. 4 | Biological consequences of the stabilization effect of small molecules. **a,b**, Confocal fluorescence images of HeLa cells (DAPI-labelled nuclei) after a heat shock treatment at 43 °C for 30 min, showing stress granules (AF488 labelled, shown as green) in cells with no pre-treatment (**a**) and in cells pre-treated with 200 mM proline for 90 min (**b**). **c**, Plot comparing the number of stress granules per cell without and with pre-treatment with 200 mM proline. $n = 112\text{--}132$ cells examined over three independent experiments. The box represents the 25th, 50th and 75th percentiles, the whiskers represent the 5th and 95th percentiles, the solid dots represent the outliers and the empty dots

represent the mean values. Significance was determined by a two-tailed Student's *t*-test ($P = 0.003$). **d**, Plot of the pharmacokinetic study to assess the bioavailability of insulin in mice comparing formulations with (blue) and without (red) proline. The data are presented as mean values over $n = 6$ replicates, and error bars are taken as 1 s.d. **e**, Plot of the area under the curve (AUC 0-t) for bioavailable insulin, as derived from the data shown in **d**; significance was determined by two-tailed Student's *t*-test ($P = 0.0109$). Scale bar, 20 μm (**a,b**).

It only requires molecules to have weak interactions with the colloids. Thus, we selected a common molecule, 1,1,1-tris(hydroxymethyl)ethane (TME), that is highly water-soluble (solubility limit >2.5 M in water²⁴) but has an exposed methyl group. As shown in Extended Data Fig. 4d, TME produces a ΔB_{22} for lysozyme in the same order of magnitude as that produced by AAs (see also SIC results; Extended Data Fig. 5b). It is also worth noting that in this TME case (Fig. 1g), the changes in PMF for AuNPs are significant. Finally, we can support the theory and especially the role of f_{\max} , by confirming the patchy model of AA interaction with proteins. As shown in Extended Data Fig. 6, both simulations and heteronuclear single quantum coherence nuclear magnetic resonance (HSQC-NMR) experiment show that proline interacts with selected residues on the solvent-exposed surface of lysozyme.

PPIs are key to the determination of the coexistence curve on protein phase diagrams, in which the equilibrium between protein-rich and protein-diluted phases is determined. A simple, commonly studied protein phase diagram is that of lysozyme²⁵, in which liquid–liquid phase separation (LLPS) is readily observed. Thus, if AAs modulate protein–protein interactions, they should affect the protein phase diagram by moving the phase-equilibrium lines upwards (destabilizing effect of AAs) or downwards (stabilizing effect of AAs). We performed cloud point measurements for lysozyme and obtained the phase diagram shown in Extended Data Fig. 7. We found that AA addition significantly alters the phase diagram of lysozyme. For clarity, we discuss hereafter the case of proline, but all changes are the same also for leucine, isoleucine, threonine, valine, alanine and glycine. The addition of 250 mM proline moves the equilibrium line in the phase diagram down as much as about 4 K for protein concentrations lower than 7.0 mM. The stabilizing effect is not limited to AAs; we show that it is also found in short

peptides, in which we find that the ΔT change on the phase line scales rather well with the concentration of the peptide units when proline is replaced by tri- or tetra-proline (Extended Data Fig. 7b), confirming the results obtained from ΔB_{22} . Furthermore, TME also has a similar effect; thus, this is not limited to biological molecules. Finally, we also find that the small molecules presented in the literature^{20–22} as stabilizing lysozyme (and discussed above) produce the expected change in cloud point temperature (Supplementary Fig. 6). For completeness, we should note that cloud point measurements were performed at low ionic strength as, when salt concentration increases, competing effects are known to arise, and they are AA dependent (Supplementary Figs. 7 and 8).

Biological effects

A major biological effect linked to protein LLPS is the formation of stress granules in cells²⁶. To test whether AAs affect LLPS, not only *in vitro* but also in a true biological system, we decided to measure the effect of proline in preventing the formation of stress granules. We chose to use heat shock to induce their formation in HeLa cells. By using fixed-cell fluorescence imaging, we observed the presence of a large amount of stress granules after the incubation at 43 °C for 30 min (Fig. 4a). When 200 mM proline was added 1.5 h before the heat shock, we observed a lower amount of stress granules (Fig. 4b). We quantified the amount of stress granules by processing images of more than 100 cells and found that the proline pre-treatment leads to a statistically significant lower average number of stress granules per cell ($P = 0.003$) (Fig. 4c). Further work indicates that the effect is common to many AAs, scales with their concentration and is present

Article

independent of the stress types, cell lines and time of addition of AAs²⁷. Therefore, we conclude that the addition of AAs hinders the formation of stress granules inside the cells. Protein–protein interactions are pervasive for the correct functioning of biological systems, so we expect that AAs will substantially affect most biological processes. As an example, we can report that the addition of glutamine strongly reduces the ability of herpes simplex virus 2 to replicate in Vero cells (Extended Data Fig. 8). Another direct consequence of modulating protein–protein interactions is that proteins will change the way they bind to each other and their propensity to form aggregates. Recently, we have demonstrated²⁸ that AAs modulate protein cross-interactions at millimolar concentrations. For example, 10 mM of glutamine reduces the binding constant of lysozyme to a whey protein isolate by one order of magnitude. In other cases, we have found changes of as much as five orders of magnitude.

It is important to state that conceptually, we show here that weak interactions lead to strong effects. The rationalization we provide for the protein stabilization of AAs should help strengthen their role in pharmaceutical formulations. To provide an example of the strength of our approach, we chose to focus on developing a new, yet simple, formulation for insulin. Insulin is a crucial therapeutic protein that exhibits a propensity for forming dimers, hexamers and larger aggregates in solution because of its substantial hydrophobic patches. The aggregation of insulin is detrimental to its therapeutic efficacy *in vivo*²⁹. There are many approaches to address this problem, but there is still a large room for improvement. At present, many research efforts have focused on formulations able to destabilize insulin aggregates³⁰. The regulation of the aggregation state of insulin is crucial not only for its bioavailability but also for its mass production, transportation and shelf life. The aggregation is predominantly associated with exogenously administered insulin and is not observed with endogenously produced insulin.

We decided to formulate insulin with proline. First, we used sedimentation velocity AUC to investigate the effect of proline on insulin aggregation. As shown in Extended Data Fig. 9, on proline addition, the hexamers of insulin tend to disappear, whereas dimers and monomers increase in concentration. Intrinsic fluorescence measurements allow us to state that proline interaction with insulin is very weak ($K_D > 10$ M). A pharmacokinetic study was undertaken to assess the impact of proline on insulin efficacy *in vivo*. In this study, 500 ng of insulin were dissolved either in saline or in saline containing 1 M proline. Each solution was administered subcutaneously to groups of six mice, with a simultaneous intraperitoneal injection of 10 mg glucose. Plasma samples were collected at various time points for insulin concentration measurement by ELISA (enzyme-linked immunosorbent assay). The results shown in Fig. 4d,e demonstrate that the inclusion of 1 M proline significantly increased the bioavailability of insulin, as evidenced by the area under the plasma concentration–time curve increasing from 63.6 ± 22.6 ng ml⁻¹ min⁻¹ to 122.5 ± 40.1 ng ml⁻¹ min⁻¹ ($P = 0.0109$). Similarly, the maximum plasma concentration markedly rose from 1.3 ± 0.3 ng ml⁻¹ to 2.6 ± 1.1 ng ml⁻¹ ($P = 0.0140$).

Outlook

The experimental data and theory presented suggest that proline has a generic colloidal effect. The AA effects presented here on B_{22} are comparable in magnitude but opposite in sign to the effects that salt has. It is accepted that salt has a generic colloidal effect that happens through the screening of the electrostatic interactions. We believe that AAs have an equally generic colloidal effect that screens attractive interactions and thus can counter the effect of salt (all the data with error bars can be found in Extended Data Fig. 10 and Supplementary Table 1).

In conclusion, we have shown that weak interactions between small molecules and patchy nanoscale colloids provide sizeable effects on the stability and the self-interactions between these colloids. This becomes

especially interesting in the case of AAs interacting with proteins, in which molar interactions lead to strong changes in the second osmotic virial coefficient and in the PMF. In turn, these changes have large effects on protein phase diagrams, liquid–liquid phase separation and binding constants. The effects shown exist for AAs as well as short peptides, both of which are abundant in cell cytosols, and we believe that their role is underappreciated. It is known that cells under osmotic pressure produce more AAs, but they also produce more peptides and AAs when they degrade intracellular proteins. Our data show that the increase in this intracellular concentration of AAs and peptides will influence all protein–protein interactions.

Online content

Any methods, additional references, Nature Portfolio reporting summaries, source data, extended data, supplementary information, acknowledgements, peer review information; details of author contributions and competing interests; and statements of data and code availability are available at <https://doi.org/10.1038/s41586-025-09506-w>.

1. Kamerzell, T. J., Esfandiary, R., Joshi, S. B., Middaugh, C. R. & Volkin, D. B. Protein–excipient interactions: mechanisms and biophysical characterization applied to protein formulation development. *Adv. Drug Deliv. Rev.* **63**, 1118–1159 (2011).
2. Liang, X., Zhang, L., Natarajan, S. K. & Becker, D. F. Proline mechanisms of stress survival. *Antioxid. Redox Signal.* **19**, 998–1011 (2013).
3. Ferreira, L. A., Uversky, V. N. & Zaslavsky, B. Y. Role of solvent properties of water in crowding effects induced by macromolecular agents and osmolytes. *Mol. Biosyst.* **13**, 2551–2563 (2017).
4. Srinivas, V. & Balasubramanian, D. Proline is a protein-compatible hydrotrope. *Langmuir* **11**, 2830–2833 (1995).
5. Arakawa, T. & Timashoff, S. N. The stabilization of proteins by osmolytes. *Biophys. J.* **47**, 411–414 (1985).
6. Yancey, P. H., Clark, M. E., Hand, S. C., Bowles, R. D. & Somero, G. N. Living with water stress: evolution of osmolyte systems. *Science* **217**, 1214–1222 (1982).
7. Ignatova, Z. & Giersch, L. M. Inhibition of protein aggregation *in vitro* and *in vivo* by a natural osmoprotectant. *Proc. Natl. Acad. Sci. USA* **103**, 13357–13361 (2006).
8. Ong, Q., Xufeng, X. & Stellacci, F. Versatile capillary cells for handling concentrated samples in analytical ultracentrifugation. *Anal. Chem.* **96**, 2567–2573 (2024).
9. Xu, X. et al. Experimental method to distinguish between a solution and a suspension. *Adv. Mater. Interfaces* **9**, 2200600 (2022).
10. Ong, Q. et al. Cryogenic electron tomography to determine thermodynamic quantities for nanoparticle dispersions. *Mater. Horiz.* **9**, 303–311 (2022).
11. Van Lehn, R. C. & Alexander-Katz, A. Ligand-mediated short-range attraction drives aggregation of charged monolayer-protected gold nanoparticles. *Langmuir* **29**, 8788–8798 (2013).
12. Jacobsen, M. P., Wills, P. R. & Winzor, D. J. Thermodynamic analysis of the effects of small inert cosolutes in the ultracentrifugation of noninteracting proteins. *Biochemistry* **35**, 13173–13179 (1996).
13. Le Brun, V., Friess, W., Schultz-Fademrecht, T., Muehlau, S. & Garidel, P. Lysozyme–lysozyme self-interactions as assessed by the osmotic second virial coefficient: impact for physical protein stabilization. *Biotechnol. J.* **4**, 1305–1319 (2009).
14. Winzor, D. J., Deszczyński, M., Harding, S. E. & Wills, P. R. Nonequivalence of second viral coefficients from sedimentation equilibrium and static light scattering studies of protein solutions. *Biophys. Chem.* **128**, 46–55 (2007).
15. Ijavi, M. et al. Surface tensiometry of phase separated protein and polymer droplets by the sessile drop method. *Soft Matter* **17**, 1655–1662 (2021).
16. Jackson, A. M., Hu, Y., Silva, P. J. & Stellacci, F. From homoligand- to mixed-ligand-monolayer-protected metal nanoparticles: a scanning tunneling microscopy investigation. *J. Am. Chem. Soc.* **128**, 11135–11149 (2006).
17. Parmar, A. S. & Muschol, M. Hydration and hydrodynamic interactions of lysozyme: effects of chaotropic versus kosmotropic ions. *Biophys. J.* **97**, 590–598 (2009).
18. Vallée-Bélisle, A. & Michnick, S. W. Visualizing transient protein-folding intermediates by tryptophan-scanning mutagenesis. *Nat. Struct. Mol. Biol.* **19**, 731–736 (2012).
19. Gutteridge, A. & Thornton, J. Conformational change in substrate binding, catalysis and product release: an open and shut case? *FEBS Lett.* **567**, 67–73 (2004).
20. Valente, J. J., Fryksdale, B. G., Dale, D. A., Gaertner, A. L. & Henry, C. S. Screening for physical stability of a *Pseudomonas* amylase using self-interaction chromatography. *Anal. Biochem.* **357**, 35–42 (2006).
21. Valente, J. J., Verma, K. S., Manning, M. C., William Wilson, W. & Henry, C. S. Second virial coefficient studies of cosolvent-induced protein self-interaction. *Biophys. J.* **89**, 4211–4218 (2005).
22. Liu, W., Bratko, D., Prausnitz, J. M. & Blanch, H. W. Effect of alcohols on aqueous lysozyme–lysozyme interactions from static light-scattering measurements. *Biophys. Chem.* **107**, 289–298 (2004).
23. Xu, X. & Stellacci, F. Amino acids and their biological derivatives modulate protein–protein interactions in an additive way. *J. Phys. Chem. Lett.* **15**, 7154–7160 (2024).
24. 1,1-Tris(hydroxymethyl)ethane, SDS initial assessment profile (2011).
25. Taratura, V. G., Holschbach, Andreas, Thurston, G. M., Blankscheit, Daniel & Benedek, G. B. Liquid–liquid phase separation of aqueous lysozyme solutions: effects of pH and salt identity. *J. Phys. Chem.* **94**, 2140–2144 (1990).

26. Mollieix, A. et al. Phase separation by low complexity domains promotes stress granule assembly and drives pathological fibrillization. *Cell* **163**, 123–133 (2015).
27. Xu, X. et al. Liquid-liquid phase separation of proteins is modulated by amino acids in vitro and in vivo. *Proc. Natl Acad. Sci. USA* **121**, e2407633121 (2024).
28. Winkler, P. M. et al. Modulating weak protein-protein cross-interactions by the addition of free amino acids at millimolar concentrations. *J. Phys. Chem. B* **128**, 7199–7207 (2024).
29. Das, A., Shah, M. & Saraogi, I. Molecular aspects of insulin aggregation and various therapeutic interventions. *ACS Bio. Med. Chem. Au* **2**, 205–221 (2022).
30. Mathieu, C., Gillard, P. & Benhalima, K. Insulin analogues in type 1 diabetes mellitus: getting better all the time. *Nat. Rev. Endocrinol.* **13**, 385–399 (2017).

Publisher's note Springer Nature remains neutral with regard to jurisdictional claims in published maps and institutional affiliations.



Open Access This article is licensed under a Creative Commons Attribution-NonCommercial-NoDerivatives 4.0 International License, which permits any non-commercial use, sharing, distribution and reproduction in any medium or format, as long as you give appropriate credit to the original author(s) and the source, provide a link to the Creative Commons licence, and indicate if you modified the licensed material. You do not have permission under this licence to share adapted material derived from this article or parts of it. The images or other third party material in this article are included in the article's Creative Commons licence, unless indicated otherwise in a credit line to the material. If material is not included in the article's Creative Commons licence and your intended use is not permitted by statutory regulation or exceeds the permitted use, you will need to obtain permission directly from the copyright holder. To view a copy of this licence, visit <http://creativecommons.org/licenses/by-nc-nd/4.0/>.

© The Author(s) 2025

Methods

Second osmotic virial coefficient

A common way to evaluate the stability of a compound in a dispersion is through the equation of state (EOS)^{8,9,31}:

$$\frac{\Pi}{kT} = \rho_2 + B_{22}\rho_2^2 + B_{23}\rho_2\rho_3 + \dots \quad (2)$$

where Π is the osmotic pressure, ρ is the number density and kT is the product of the Boltzmann constant (k) and the temperature (T). In this equation, B is the virial coefficient, with the subscript numbers indicating the component of the dispersion—1 for the solvent, and 2 and 3 for the main and minor solute. Therefore, B_{22} is the osmotic second virial coefficient that measures the self-interaction among the main solutes. When all virial coefficients have a value of 0, the EOS becomes equivalent to that for the ideal gas. A virial expansion is needed to represent realistic dispersions.

Origin of the energy landscape in the PMF of the nanoparticle

For nanoparticles, we observe a peak in the PMF at around twice the diameter D , and the height and position are concentration dependent. Given its range, this peak indicates that a longer-range attractive force is at play. The origin of the peak comes from the competition between the well-known plasmonic coupling between gold nanoparticles and a screened Coulomb repulsive force between the charged particles. The strong attractive well is due to ligand–ligand contact interactions. A sketch of all the interactions at play is shown in Supplementary Fig. 9. Previous calculations by our group have estimated the depth of the well for similar-sized nanoparticles (neglecting plasmons) to be of the same order of magnitude as that measured in this paper¹¹. This deep well should not be affected by the presence of AAs. However, at distances above the contact point, there is an attractive contribution to the potential due to electrostatic dipole–dipole couplings in the form of plasmon coupling.

Exclusion of other mechanisms

As directly demonstrated by SIC (Fig. 2b), we measure positive changes in ΔB_{22} at AA concentrations as low as 10 mM, corresponding to a molar ratio of lysozyme to AA of about 1:7 (shown for glutamine in Supplementary Fig. 10, representative for all AAs). We performed a classical hydrotrope assay³², in which the solubility of a hydrophobic compound (fluorescein diacetate, FDA) in water is measured as a function of hydrotrope concentration. As shown in Supplementary Fig. 5, we did not find a threshold concentration for proline as the minimum hydrotrope concentration. Furthermore, we tested ΔB_{22} dependence on the absolute concentration of the AA or on the stoichiometric ratio between the AA and the protein. We found that ΔB_{22} depends only on the absolute AA concentration and not on that of the proteins (Supplementary Fig. 11).

Theoretical framework

For the simplicity of presentation, we discuss below the case of AAs interacting with proteins, but the model is general and is developed for small molecules interacting with nanoscale colloids in a dispersion. Consider a set of n colloidal particles with z attractive patches, with which they can interact with other identical colloidal particles. Given the coordination number z , we can think of this problem as that of colloids in a lattice with coordination given by z . We set the volume of a lattice point to be approximately the volume of the colloids a^3 , for simplicity. The coordination number depends on the number of patches and is an open variable, but it will generally be a number of order 10 or less (for example, the coordination number for a face centre cubic lattice would be 12, but it is 2 for divalent patchy particles). The coordination number sets the fictitious lattice on which we will work, but it is not important for the rest of our calculations, nor does it have

further implications. The energy between two colloids is considered to have strong short-range repulsion (hard core), short-range attraction between patches (hydrophobic effect), screened long-range repulsion (electrostatic) and longer-range attraction from dipole–dipole interactions (Supplementary Fig. 9). This model is analogous to the DLVO theory. The increase in B_{22} can be obtained by screening the short- or long-range attraction, which, in turn, increases the effect of repulsive forces. The latter, longer-range attractive term is important in the case of polarizable gold nanoparticles. In this case, the adsorption of zwitterionic AAs onto the ligand shell will screen NP–NP attractive dipole–dipole interactions, but leave the repulsion for the most part untouched, given that the excess AAs will be within the ligand shell because of hydrophobic attraction.

For simplicity, we will start with purely short-range interactions, which are applicable to most proteins. For this case, the free energy (per site) can be constructed directly from a mean-field (Bragg–Williams) approach to yield

$$\frac{\Delta G}{kT} = \phi \ln \phi + (1 - \phi) \ln(1 - \phi) + \chi \phi(1 - \phi) \quad (3)$$

where ϕ is the volume fraction of the colloids within the solvent. The interaction is completely captured by the incompatibility parameter χ (normally referred to in soft matter as the Flory χ parameter)

$$\chi = \frac{z}{kT} \left(\epsilon_{CS} - \frac{\epsilon_{SS} + \epsilon_{CC}}{2} \right) \quad (4)$$

where the different ϵ values represent an effective interaction energy (per patch) of either colloid–colloid (CC), solvent–solvent (SS) or the cross-interaction colloid–solvent (CS). As can be seen from equation (4), increasing (or decreasing) the incompatibility parameter χ , which dictates the enthalpy of mixing, can be accomplished by increasing (decreasing) the strength of the interactions ϵ values, or by changing the effective coordination of the colloids z . We believe that the mechanism by which AAs modulate the colloid–colloid interaction is a competition-type of interaction, meaning AAs decrease z by blocking attractive patches and hydrating them. This is seen in the PMF of apoferritin (Fig. 1f), in which the short-range attractions disappear on increasing the concentration of AAs. The second virial coefficient can be extracted from the expansion of the free energy, and is written as

$$B_{22} = a^3(1 - 2\chi) \quad (5)$$

Note that in the absence of attractive interactions (that is, $\chi \rightarrow 0$), the excluded volume becomes the lattice site volume. More generally, we should evaluate the second virial as $B_{22} = -\frac{1}{2} \int (e^{-U/kT} - 1) d\mathbf{r}$, where U is the pair interaction potential. It is important to note that in the model we are studying, the attractive interaction parametrized by χ is assumed to be a contact interaction of very short range, that is, a contact interaction occurring only on contact with the particles, and this gives rise to the interacting part scaling with a^3 . This is a good approximation in the limit that the interactions are short ranged, which we believe applies to proteins under biological conditions. However, if long-range electrostatic repulsive or attractive interactions are present, we would need to add a constant to the virial potential and express it as

$$B_{22} \approx a^3 \left(1 + \frac{1}{a^3} \Delta B_{22}^{\text{elec}} - 2\chi \right) \quad (6)$$

where $\Delta B_{22}^{\text{elec}} = -\frac{1}{2} \int_a^\infty (e^{-U_{\text{elec}}/kT} - 1) d\mathbf{r}$. For a pure Coulomb potential, we find that $\Delta B_{22}^{\text{elec}}$ does not converge, but it does for a Debye–Yukawa potential, which is expected under the conditions typically encountered in colloidal solutions. As can be seen from equation (6), this generalized form of the second virial coefficient is similar to the original

case where no electrostatic contributions were assumed. We need to rescale only the effective size of the colloid by the effective repulsive excluded volume and rescale the attractive part accordingly. Thus, for simplicity, we will assume from here on equation (6) without losing generality, with the understanding that a^3 corresponds to an effective excluded volume and not just the steric contribution. As will be seen below, this rescaling does not affect any of our results.

Now we turn our attention to the effect of AAs or similar small molecules. We assume that AAs adsorb onto some patches of the proteins, which is in agreement with literature reports that have observed the adsorption (that is, weak interaction) of some AAs onto protein surfaces^{33–36}. The adsorption is transient, but it equilibrates rapidly because the barriers to adsorb and desorb are small, and the diffusion constant of the AAs is large compared with that of the proteins themselves^{37,38}. Thus, we can think of this system as consisting of an adsorption onto a surface with Nz adsorption sites, where N is the number of proteins and each has z patches to adsorb onto. We will assume, for simplicity, that one patch can only adsorb one AA or small molecule. This is not a strict condition and can be easily relaxed by assuming each patch has a given number of adsorption sites. We can model this adsorption process using the Langmuir adsorption isotherm, in which we can compute the fractional coverage (fraction of adsorbed sites) as

$$\theta = \frac{Kc}{1 + Kc} \quad (7)$$

where c is the concentration of AAs and K is the equilibrium constant of binding between AAs and attractive patches. These quantities can be measured or computed.

The effective coordination is then given by $z = z_0(1 - \theta)$, with z_0 being the original number of patches in the absence of AAs. Finally, the second virial coefficient becomes

$$B_{22} \approx a^3 \left(1 - 2 \frac{z_0}{kT} (1 - \theta) F(\{\epsilon\}) \right) \quad (8)$$

where $F(\{\epsilon\})$ is a function that depends only on the original interaction parameters and is independent of the concentration of AAs.

The second virial coefficient in the absence of AAs (when $\theta = 0$) can be written as

$$B_{22}^0 \approx a^3 \left(1 - 2 \frac{z_0}{kT} F(\{\epsilon\}) \right) \quad (9)$$

and the change in the virial coefficient on addition of AAs is then simply given by

$$\Delta B_{22} \sim 2a^3 \frac{z_0}{kT} \theta F(\{\epsilon\}) \quad (10)$$

Inserting the expression of B_{22}^0 in terms of $F(\{\epsilon\})$ in ΔB_{22} from equation (9) and explicitly considering the fraction of sites, we find that the change of the second virial coefficient is an expression independent of the interaction energies:

$$\Delta B_{22} = (a^3 - B_{22}^0) \frac{Kc}{1 + Kc} \quad (11)$$

This expression is insightful because it shows that the scale of change in the second virial is dictated by the difference between the maximum excluded volume the colloid can have given by a^3 (stemming from purely repulsive interactions, steric + electrostatic, as discussed above), and the measured and actual excluded volume in the absence of AAs, that is, B_{22}^0 that does include the effect from attractive patches. The change is regulated by the number of blocked attractive sites and patches given by the Langmuir expression, in which the equilibrium constant K can be extracted by fitting. It is important to mention that

we are treating all patches equally. This condition can be relaxed (as shown below) and does not affect the results we are presenting. Furthermore, this relationship allows the quantification of the strength of the interaction that will lead to noticeable changes; these will happen when the product of K and c is in the range of 1.

We further introduce f_{\max} , a small molecule-dependent parameter that captures the intrinsic affinity of a molecule to cover the surface of a particle. As shown in Fig. 2a,b, the plateau for proline-stabilized lysozyme is almost twice that of glycine-stabilized lysozyme. The assumption implicit in the Langmuir model that results in equation (11) is that the whole surface is made of identical patches and all small molecules will take ΔB_{22} to the same plateau at infinite concentration. This is not observed experimentally. f_{\max} is the maximum fraction of the surface that a small molecule can cover. In other words, it is the fraction of patches in the surface to which the small molecule can adsorb. Equation (11) becomes

$$\Delta B_{22} = (a^3 - B_{22}^0) \frac{Kc}{1 + Kc f_{\max}} \quad (12)$$

It is important to note that we have made some approximations, namely, we have assumed that all the patches are equal and have the same interaction energy. This implies that we are not distinguishing the actual orientation of the bonds between colloids, nor the relative difference in interaction between different patches and the solvent. Although this is not true in general, we can think of the interacting patches that drive aggregation as a subset of patches and can lump the contributions of the other patches onto an effective interaction parameter that is not affected by the presence of the AAs. This can be calculated explicitly by considering, for example, two different subsets of patches. The total number of patches $z = z_1 + z_2$, and the respective interactions will be ϵ_{SS} , ϵ_{CS}^1 , ϵ_{CS}^2 , $\epsilon_{CC}^{1,1}$, $\epsilon_{CC}^{2,2}$, $\epsilon_{CC}^{1,2}$. Invoking the mean-field approximation as used above, we obtain the same free energy form with

$$\chi = \frac{z}{k_B T} \left(f_1 \epsilon_{CS}^1 + f_2 \epsilon_{CS}^2 - \frac{\epsilon_{SS} + (f_1^2 \epsilon_{CC}^{1,1} + f_2^2 \epsilon_{CC}^{2,2} + 2f_1 f_2 \epsilon_{CC}^{1,2})}{2} \right) \quad (13)$$

where $f_1 = z_1/z$ and $f_2 = z_2/z$, with the condition $f_1 + f_2 = 1$. Regrouping this equation, we can see that if, for example, patches of type 1 can be screened by the AAs, whereas patches of type 2 will not, then

$$\chi = \chi_1 + \Delta\chi \quad (14)$$

where

$$\chi_1 = \frac{z}{k_B T} \left(f_1 \epsilon_{CS}^1 - \frac{f_1^2 \epsilon_{SS} + (f_1^2 \epsilon_{CC}^{1,1})}{2} \right) \quad (15)$$

The $\Delta\chi$ term does not change on adding AAs, so the aforementioned change in the second virial coefficient holds, even if the total χ parameter is negative from $\Delta\chi$, in the approximation of χ_1 being much smaller than $\Delta\chi$.

Cloud point determination

The critical temperatures (T_{cr}) and critical lysozyme concentrations (C_{cr}) were found by fitting the coexistence curves by the following equation (11):

$$\text{Cloud point} = T_{cr} \left(1 - \alpha \left(\frac{C_{cr} - C_p}{C_{cr}} \right) \right)^{\frac{1}{\beta}} \quad (16)$$

where C_p is the protein concentration; $\beta = 0.33$ is the critical exponent; and α , T_{cr} and C_{cr} are the adjustable parameters³⁹.

Article

A 20 mg ml⁻¹ lysozyme solution in 1× PBS was filtered through a 0.45-μm syringe filter and concentrated in Amicon tubes (10 kDa cut-off, Ultra-15) by centrifuging at 5,000 rpm at 20 °C for 50 min. Lysozyme concentration was measured by Implen NanoPhotometer (Implen) at 280 nm using an extinction coefficient of 2.72 mg⁻¹ ml cm⁻¹. The concentration of the lysozyme stock solution was adjusted to 200 mg ml⁻¹. The stock solutions of the AAs were prepared by dissolving the amino acid powder in water (Milli-Q) until a final volume of 1 ml was reached and adding 1 ml of 2 M NaCl solution in 2× PBS. The two-fold serial dilution of the stock solutions of AAs was done in 1 M NaCl solution in 1× PBS. Mixing of protein and amino acid solutions as well as transferring of the samples (100 μl) to capillaries (0.3 ml Crimp Neck Micro-Vial, 31.5 × 5.5 mm, clear glass, round bottom) were performed in ThermoMixer F1.5 Eppendorf at 42 °C. The blocks in a CrystalBreeder (Technobis Crystallization Systems) were kept at 42 °C for 10 min before the capillaries were placed into the instrument. The transmissivity was calibrated automatically after 5 min of temperature equilibration of the sample at 42 °C, followed by cooling down at a rate of 0.2 °C min⁻¹ under constant nitrogen flow to prevent protein oxidation. The cloud point temperature was registered at 70% transmissivity loss.

Detailed synthesis and characterization

Hen egg-white lysozyme (14.3 kDa, ≥95%) was purchased from Roche. All the AAs were purchased from Thermo Scientific in powder form. FUS-LCD was a gift from Prof. Dufresne¹⁵. BSA was purchased from Thermo Scientific. Ferritin and apoferitin were ordered from Sigma-Aldrich. Poly-proline peptides (tri- and tetra-proline) were purchased from Bachem Americas. 1,1,1-Tris(hydroxymethyl)ethane (TME, 97%) was purchased from ABCR Swiss. Plasmid DNA (4207 bp dsDNA, pIVEX1.3-CAT) was purchased from Biotechrabbit. The salts for the sodium phosphate buffer were also purchased from Sigma-Aldrich in powder form.

Synthesis of nanoparticles

HAuCl₄·3H₂O (789.3 mg), oleylamine (64 ml) and *n*-octane (80 ml) were mixed in a 500 ml three-necked round-bottom flask. The mixture was left stirring till the solid completely dissolved. The flask was connected to argon flow for 10 min followed by a quick injection of 16 ml of *tert*-butylamine-borane complex (351.3 mg) dissolved in oleylamine to induce the reduction reaction. The reaction was constantly stirred for 1 h and quenched with 240 ml of ethanol. Nanoparticles were precipitated with centrifugation. This was followed by sonication adding fresh dichloromethane and then ethanol several times and reprecipitated each time before adding fresh ethanol to remove organic residuals from reaction materials. Oleylamine (90 mg) functionalized nanoparticles was dissolved in 30 ml dichloromethane (dissolved with 34.86 mg of sodium mercapto-undecane sulphonate (MUS) and 31.23 μl of octane thiol). The ligand exchange was kept sealed and under stirring for 21 h. The nanoparticles after ligand exchange were sonicated and precipitated several times with fresh dichloromethane and acetone to remove organic residuals. Then pre-purified nanoparticles were dissolved in ultrapure water using Amicon 30 kDa MWCO filters for further purification to remove MUS. NMR of nanoparticles is presented in Supplementary Fig. 1 to show the quality of purification as well as the final composition of the two ligands functionalized on the nanoparticles.

Purification of ferritin based on sucrose density gradient ultracentrifugation

Ferritin, from equine spleen type I (Sigma-Aldrich, in saline solution), known to have a wide distribution of ferritin because of different iron loads, oligomerization or apoferitin impurities⁴⁰, was purified using preparative ultracentrifugation. Sucrose gradients in Milli-Q water (5–30 wt%) were prepared in six ultracentrifuge tubes (Ultra-Clear, 25 × 89 mm, SW28, Beckman Coulter, USA) by a Piston Gradient Fractionator (BioComp Instruments). Ferritin solution (400 μl) was loaded

onto the gradient, followed by centrifuging (Optima XPN-80, Beckman Coulter) in a SW32 rotor, followed by centrifugation at 30,000 rpm at 20 °C for 2 h. Then three fractions were collected in a top-down manner (the liquid surface being 0 mm), at distances of 20–28 mm (fraction 1), 28–36 mm (fraction 2) and 36–46 mm (fraction 3). Each fraction was purified five times with 1× PBS in Amicon tubes (100 kDa cut-off, Ultra-15), at 4,000 rpm, 4 °C for 30 min. Quality of purification were characterized by analytical ultracentrifugation in sedimentation velocity (AUC-SV) (Supplementary Fig. 12). For AUC-SV, 380 μl of 1× PBS (reference) and 376 μl of the sample were loaded into 12 mm cells in an An60-Ti rotor and equilibrated at 20 °C in vacuum for 2 h, followed by velocity scans at 15,000 rpm with an absorbance profile collected at 280 nm. Data analysis was done using SEDFIT software⁴¹ with maximum entropy regularization at a confidence level of 0.68, final s-resolution of 500 in s-interval from 0 S to 250 S. For the cryo-EM measurement, fraction 2 was chosen due to its relatively monomeric distribution at around 60 S that is typical for ferritin⁴⁰ (Supplementary Fig. 12). Concentration of ferritin was measured by Implen NanoPhotometer (Implen) at 420 nm using an extinction coefficient⁴² of 10 mg⁻¹ ml cm⁻¹.

Cryogenic transmission microscopy

A total of 3.5 μl of dispersion was cast onto a previously glow-discharged quantifoil grid (Quantifoil R1.2/1.3, 200 Mesh, Cu). The grid with solution was blotted with Whatman filter papers on both sides in a vitrobot (Vitrobot Mark IV) at 100% humidity and 22 °C, followed by immediate vitrification in liquid ethane. Imaging was performed at the Dubochet Center for Imaging (Lausanne) using a Titan Krios G4 microscope operating at 300 kV. Tilt series were recorded from -60° to 60° with two increments at a magnification of 33,000× (camera pixel size of 0.37 nm), a defocus of about 7 μm and a total dose of 120 e⁻ Å⁻². For data processing, pre-aligned .mrc files were compiled from Tomography v.5.16.0 (Thermo Fisher Scientific) and Camera Falcon 4i equipped with Selectris X energy filter (slit width 20 eV).

Generating PMF curves from cryo-ET tomograms

Details of this workflow were published in ref. 10. The contrast of the tomogram was inverted using ImageJ (NIH). High-contrast nanoparticles became white in the tomogram. Extra slices on the bottom and top of the tomograms, where there were no particles, were trimmed away to reduce the size of the tomogram. The tomogram was exported as a whole in the mrc file format and then imported into Imaris (Bitplane) for visualization and segmentation in *.ims format. The segmentation to detect particles was performed by following the steps of the built-in Surface detection function in Imaris, with seed growth selection turned on to dissect particles that are close to each other. The coordinates of the detected particles were exported to a text file and further processed for flatness and tilt correction. A rectangular box containing particles were cropped out and used for calculation of the radial distribution function. The particle coordinates are exported to the final text file that contains three columns; each row contains a 3D position (*x*, *y*, *z*) for a particle. It is read into the previously published Python program to calculate the radial distribution function. The PMF is found to be the logarithm of this function multiplied by thermal energy *K_BT*. Typical tomograms and their segmentation are shown in Supplementary Figs. 13–15.

Column grafting for SIC experiments

For this work, we adapted and optimized the experimental procedure for the custom-made column grafting with lysozyme and the protocol established in ref. 13 for our SIC experiments. For the grafting of the SIC column, a Tricorn 5/50 column (Cytiva, Column Volume of 1.178 ml) was manually grafted with lysozyme (Lys) using TOYOPEARL AF Formyl-650M chromatography particles, sodium cyanoborohydride, potassium phosphate and ethanolamine as a resin. The standard buffer used throughout the experiments was 50 mM sodium phosphate

at pH ≈ 6.9, consisting of monobasic and dibasic sodium phosphate in MilliQ water.

All experiments were performed on SIC columns with a grafted surface coverage of lysozyme of around 45%. The column was packed under pressure with the following flow rates: 0.75 ml min⁻¹ for 15 min, then at 3 ml min⁻¹ at 15 min and again at 0.75 ml min⁻¹ for 30 min. The column was stored at 4 °C overnight and between experiment days.

SIC experiments

To prepare a chromatography column for a CIC experiment, Lys was manually grafted on the column, as outlined in the previous section, and for the optimized signal-to-noise ratio of the elution profile, we determined that the protein concentration should be around 20 mg ml⁻¹, which was injected in all SIC experiments in this work.

SIC experiments were conducted to probe the Lys self-interaction in different solution environments (buffer alone or in the presence of small molecules, such as AAs, poly-proline and TME at different concentrations dissolved in buffer) from which the respective values of B_{22} were calculated. Before each measurement series, a column performance test was run with 20% acetone in Milli-Q water. For each run of the experiments, 50 µl of lysozyme at 20 mg ml⁻¹ was injected. Samples were injected after 10× column volume and with a constant flow rate of 0.75 ml min⁻¹ at room temperature. The AAs tested were proline, glycine, serine, threonine, asparagine and glutamine, and their concentration was varied between 5 mM and 1.2 M (considering their respective solubility limit). The upper range limit was set by the fact that towards the solubility limit of an added molecule (for example, amino acid, polyproline peptides, TME), the buffer solution becomes turbid, which very likely clogs and thus breaks the column. Therefore, to protect the grafted column, we set the upper limit to 1.2 M, a range well below the solubility limit of the studied AAs and small molecules.

Determination of B_{22} by SIC

In SIC experiments, we evaluate the interactions between the injected protein in the mobile phase and the immobilized protein grafted on the column in terms of the measured retention volume. To experimentally determine B_{22} , we first compute the retention factor $k' = (V_0 - V_R)/V_0$, where V_0 is the retention volume of non-interacting species, which is calculated before each experiment with the column performance test using 20% acetone in MilliQ water and V_R is the volume required to elute the injected protein in the mobile phase through the grafted column. Then B_{22} (mol ml g⁻²) can be computed as

$$B_{22} = B_{HS} - k's\phi \quad (17)$$

where $B_{HS} = 2\pi r^3/3N_A M^2$ is the excluded volume or hard-sphere contribution of the two interacting proteins, assuming a spherical shape, s is the immobilization density, that is, the number of covalently immobilized protein molecules per unit area of the bare chromatography particles and $\phi = A_s V_0$ is the phase ratio (that is, the total surface available to the mobile phase protein). To calculate B_{HS} , we used the hydrodynamic radius r (1.89 ± 0.03 nm) and the average molecular weight $M = 14,300$ g mol⁻¹ of the self-interacting lysozyme¹⁷; N_A is Avogadro's number. To exchange the units for B_{22} (mol ml g⁻²), which is commonly used in SIC experiments, to one of the AUC experiments B_{22} (m³) = B_{22} (mol ml g⁻²) $M/N_A 10^{-6}$.

The assumption here is that we measure only two-body interactions, that is, one injected free protein interacts with only one immobilized protein molecule at a time. This constraint can be guaranteed by controlling the immobilized proteins grafted onto an effectively flat surface being the column. Another assumption is that the injected free Lys interacts only with one immobilized Lys grafted onto the column and not with each other. This can be verified by determining the variation for the calculated B_{22} value measured at a concentration of 5–30 mg ml⁻¹ of the lysozyme. For the Lys–Lys self-interaction, the obtained B_{22} value

should remain constant. We determined this variation to be about 3.4×10^{-26} m³ for Lys–Lys and considered this variation in our error analysis.

Sedimentation diffusion equilibrium analytical ultracentrifugation

In a typical SE-AUC experiment, a protein solution in phosphate buffer (pH 7, 50 mM) at a typical concentration of 10 mg ml⁻¹ was mixed with AAs. The final solutions were added into the AUC cells (3 mm path-length). Gold nanoparticles were measured using capillary cells⁸. The sedimentation diffusion equilibria with a depleted meniscus at a proper angular velocity, 20 °C were reached typically after 24 h. The protein concentration gradient was obtained and converted into the EOS curve by the previously established methods⁹.

Intrinsic fluorescence measurements of lysozyme

All fluorescence measurements were performed with the CaryEclipse fluorometer (Agilent) using a 1.0-cm quartz cuvette. The fluorescence spectra of lysozyme (10 µM) with variable concentrations of proline (0–1 M), glycine (0–1 M), serine (0–1 M) and alanine (0–1 M) were measured at a constant temperature (25 °C). The volumes of the samples were adjusted to 1.5 ml with 50 mM sodium phosphate buffer, at pH = 6.9. The samples were excited at 290 nm, and the fluorescence was recorded from 310 nm to 420 nm with an em/ex slit of 5 nm and a scanning speed of 120 nm min⁻¹.

If it is assumed that there are similar and independent binding sites in the protein, the binding constant (K_D) and the number of binding sites (n) can be determined using the following equation^{43,44}:

$$\log\left(\frac{F_0 - F}{F}\right) = \log K_D + n \log(Q) \quad (18)$$

where F_0 and F are the fluorescence intensities in the absence and presence of AAs, respectively. Q is the quencher concentration, for example, amino acid. k_D and n can be determined by the intercept and the slope of the linear regression of $\log\left(\frac{F_0 - F}{F}\right)$ compared with $\log(Q)$.

Dynamic light scattering

Lysozyme and BSA solutions, about 0.8 mg ml⁻¹, in phosphate buffer (pH 7, 50 mM) were filtered (0.22 µm) before DLS measurements using Nano ZS from Malvern. All DLS measurements were performed with three replicates.

Sedimentation velocity AUC study of insulin aggregates

Before AUC-SV experiments, insulin was dissolved in a glass vial containing saline (NaCl 0.9%) and in a glass vial containing saline (NaCl 0.9%) with 1 M proline, respectively. The two vials were subjected to mechanical mixing in identical conditions in a tilting shaker at the same time and for the same duration of 1 h. Clear saturated insulin solutions were obtained by brief low-speed centrifugation of the vials to remove large visible aggregates. AUC-SV measurements were performed immediately afterwards in a Beckman Coulter Optima XL-I analytical ultracentrifuge equipped with an AN-60 rotor. Two-sector cells with a titanium centrepiece (path length of 12 mm, Nanolytics) and sapphire windows were used. The AUC was stabilized at least 2 h before start. The experiments were conducted at 20 °C at 60,000 rpm, in absorbance mode with no delay set between scans. Sedfit (v.17.0) was used to fit the experimental data to obtain the distribution of sedimentation coefficients $C(s)$, which was then displayed by GUSSI.

Cell culture

HeLa cells (CCL-2) were cultured in Dulbecco's modified Eagle medium (high glucose, GlutaMAX supplement), supplemented with 10% foetal bovine serum and 1% penicillin–streptomycin. The cells were cultured at 37 °C, 5% CO₂.

Immunofluorescence microscopy

The HeLa cells were plated in an ibidi 8-well μ -Slide at a seeding density of 1.5×10^4 cells ml^{-1} 24 h before the experiment. The cell culture media were replaced with fresh cell culture media supplemented with 200 mM of proline and incubated at 37 °C, 5% CO₂ for 1.5 h. The cells were then incubated at 43 °C, 5% CO₂ for 30 min for the heat shock treatment and fixed with 4% formaldehyde phosphate-buffered saline (PBS) for 15 min. The fixed cells were then permeabilized with 0.25% Triton X-100 in PBS for 15 min and blocked with 20 mg ml^{-1} bovine serum albumin in PBS. The cells were first incubated overnight at 4 °C with the primary antibody, mouse anti-G3BP mAb (1:300, Abcam) and then incubated for 45 min at room temperature with the secondary antibody Alexa Fluor 488 (AF488) goat anti-mouse IgG (1:300, Abcam). Then cell nuclei were stained with 4',6-diamidino-2-phenylindole (DAPI) (1:1000, Sigma-Aldrich) for 15 min at room temperature and F-actin was stained by Alexa Fluor 555 Phalloidin (1:500, Thermo Fischer) for 35 min at room temperature. The fixed cells were then imaged using the Leica SP8 inverted confocal microscope with a 63× oil-immersion objective (NA = 1.40, HC PL APO, Leica). All z-stack images were acquired with the same z-step size of 1 μm and the same pixel dwell time of 3.16 μs .

Pharmacokinetic study

For the pharmacokinetic study, 500 ng of insulin was dissolved in saline or with 1 M proline in saline. Each group consisted of 5 mice, which were administered the solution by subcutaneous injection. Simultaneously, 10 mg of glucose was administered intraperitoneally. Mouse plasma was collected at various time points, and insulin concentrations were measured at these different time points using ELISA kits. The pharmacokinetic parameters were fitted using a non-compartmental analysis of plasma data after extravascular input using the package PK-solver.

Animal care

All animal procedures were performed in compliance with protocols approved by the Animal Care and Use Committee of the Southern University of Science and Technology (resolution number: SUSTech-JY202407031). During all animal experiments, the Chinese law and the local Ethical Committee Quantita Protocol were followed.

Details on ELISA detection

The ELISA kit used for insulin detection was purchased from Solarbio (catalogue no. SEKH-0219). Thirty minutes before the experiment, the reagent kit was allowed to return to room temperature. Before starting, the enzyme-linked plate was soaked three times and patted dry. Standard and test samples (100 μl each) were added to the reaction wells. The plate was sealed and incubated with shaking at room temperature (25 ± 2 °C) for 120 min, then washed plate four times and patted dry. Biotinylated antibody working solution (100 μl) was added to the reaction wells. The plate was sealed and incubated with shaking at room temperature (25 ± 2 °C) for 60 min, then washed four times and patted dry. Enzyme conjugate working solution (100 μl) was added to the reaction wells. The plate was sealed and incubated with shaking at room temperature (25 ± 2 °C) for 30 min, then washed five times and patted dry. Chromogenic substrate (100 μl) was added to the reaction wells. The plate was sealed and the colour developed in the dark at room temperature (25 ± 2 °C) for 5–20 min. Stop solution (50 μl) was added and the OD value at a wavelength of 450 nm measured within 5 min using an ELISA reader.

Reporting summary

Further information on research design is available in the Nature Portfolio Reporting Summary linked to this article.

Data availability

The data provided in the main text or the supplementary materials are found at Zenodo⁴⁵ (<https://doi.org/10.5281/zenodo.15315431>).

31. Van Rijssel, J. et al. Size-dependent second virial coefficients of quantum dots from quantitative cryogenic electron microscopy. *J. Phys. Chem. B* **118**, 11000–11005 (2014).
32. Patel, A. et al. ATP as a biological hydroprobe. *Science* **356**, 753–756 (2017).
33. Liao, Y.-T., Manson, A. C., DeLyser, M. R., Noid, W. G. & Cremer, P. S. Trimethylamine N-oxide stabilizes proteins via a distinct mechanism compared with betaine and glycine. *Proc. Natl. Acad. Sci. USA* **114**, 2479–2484 (2017).
34. Ganguly, P. et al. Cosolvent exclusion drives protein stability in trimethylamine N-oxide and betaine solutions. *J. Phys. Chem. Lett.* **13**, 7980–7986 (2022).
35. Kita, Y., Arakawa, T., Lin, T.-Y. & Timasheff, S. N. Contribution of the surface free energy perturbation to protein-solvent interactions. *Biochemistry* **33**, 15178–15189 (1994).
36. Arakawa, T. et al. Suppression of protein interactions by arginine: a proposed mechanism of the arginine effects. *Biophys. Chem.* **127**, 1–8 (2007).
37. Polson, A. On the diffusion constants of the amino-acids. *Biochem. J.* **31**, 1903–1912 (1937).
38. Yu, M. et al. The investigation of protein diffusion via H-cell microfluidics. *Biophys. J.* **116**, 595–609 (2019).
39. Muschol, M. & Rosenberger, F. Liquid-liquid phase separation in supersaturated lysozyme solutions and associated precipitate formation/crystallization. *J. Chem. Phys.* **107**, 1953–1962 (1997).
40. Ghirlando, R., Mutskova, R. & Schwartz, C. Enrichment and characterization of ferritin for nanomaterial applications. *Nanotechnology* **27**, 045102 (2016).
41. Schuck, P. Size-distribution analysis of macromolecules by sedimentation velocity ultracentrifugation and Lamm equation modeling. *Biophys. J.* **78**, 1606–1619 (2000).
42. May, M. E. & Fish, W. W. The UV and visible spectral properties of ferritin. *Arch. Biochem. Biophys.* **190**, 720–725 (1978).
43. Liu, H. et al. Competitive binding of synergistic antioxidant chlorogenic acid and (-)-epigallocatechin gallate with lysozyme: insights from multispectroscopic characterization, molecular docking and activity evaluation. *J. Mol. Liq.* **341**, 117387 (2021).
44. Zhan, M., Guo, M., Jiang, Y. & Wang, X. Characterization of the Interaction between gallic acid and lysozyme by molecular dynamics simulation and optical spectroscopy. *Int. J. Mol. Sci.* **16**, 14786–14807 (2015).
45. Siri. (2025). Datasets for amino acids stabilizing effect on protein and colloidal dispersions. Zenodo <https://doi.org/10.5281/zenodo.15315431>.

Acknowledgements This work was supported by the Swiss National Science Foundation, Horizon 2020 Research and Innovation program of the European Union under grant agreement no. 101017821 (LIGHT-CAP), and the Nestlé Research Foundation. We thank Y. Yang, H. Wang, S. Guldin, A. Murello, P. Arosio, L. Faltová, J. Aragones and F. Sciorino for their discussions. A.A.-K. thanks the Michael and Sonja Koerner Chair for the support. We thank H. Wang for performing the stress granule experiments. The cryo-EM data collection and initial image processing were performed at the Dubochet Center for Imaging Lausanne (a joint initiative of EPFL, UNIGE, UNIL and UNIBE) with the assistance of A. Myasnikov, B. Beckert, S. Nazarov, I. Mohammed and E. Uchikawa.

Author contributions Q.O. and F.S. conceived and supervised the project. A.A.-K., F.S. and Q.O. developed the theory. Q.O., T.M., X.X., P.M.W., C.S. and E.P. designed and carried out the experiments and analysed the results. Z.L. designed the pharmacokinetic studies and N.X. and Y.H. carried them out. K.A.Z. performed the MD simulations. R.L.P. studied the reduction of viral replication. P.J.S. synthesized the ligands and was the first to identify the effect of solvents on the stability of dispersions that catalysed the start of this work. Z.L. was the first to identify the effect of AAs on dispersions. X.X. performed SE-AUC experiments and B_{22} data analysis and the stress granule studies. All authors discussed the results and co-wrote the paper.

Competing interests The authors declare no other competing interests.

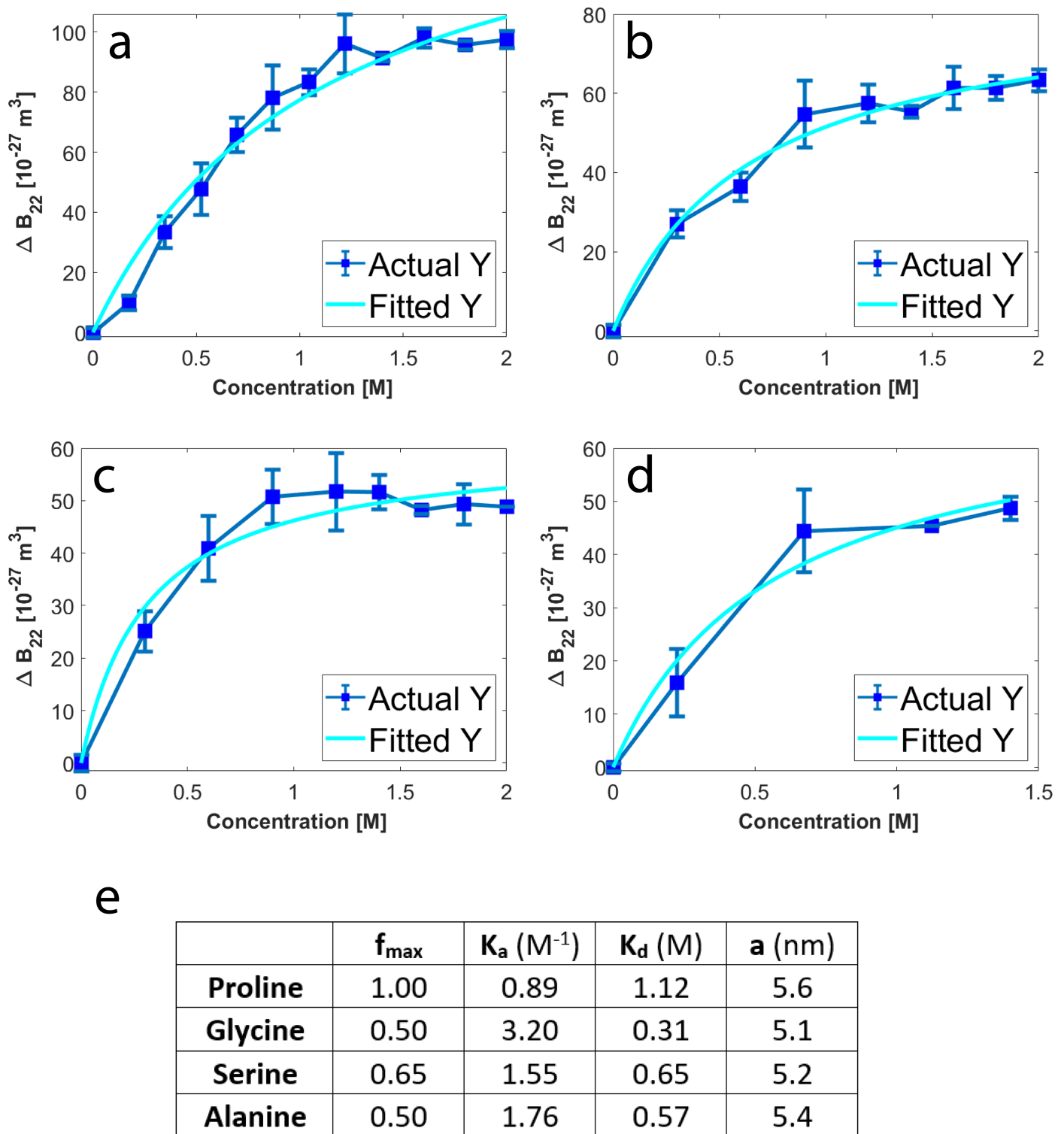
Additional information

Supplementary information The online version contains supplementary material available at <https://doi.org/10.1038/s41586-025-09506-w>.

Correspondence and requests for materials should be addressed to Zhi Luo, Quy Ong, Alfredo Alexander-Katz or Francesco Stellacci.

Peer review information *Nature* thanks Eric Appel, Nico van der Vegt and the other, anonymous, reviewer(s) for their contribution to the peer review of this work.

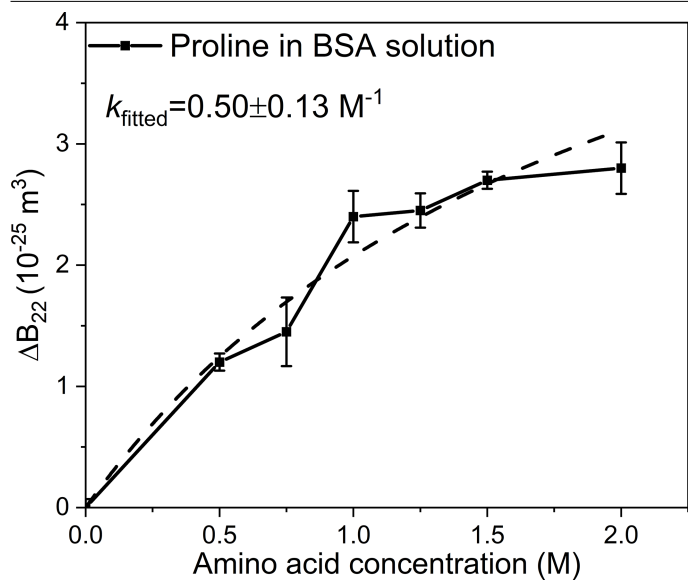
Reprints and permissions information is available at <http://www.nature.com/reprints>.



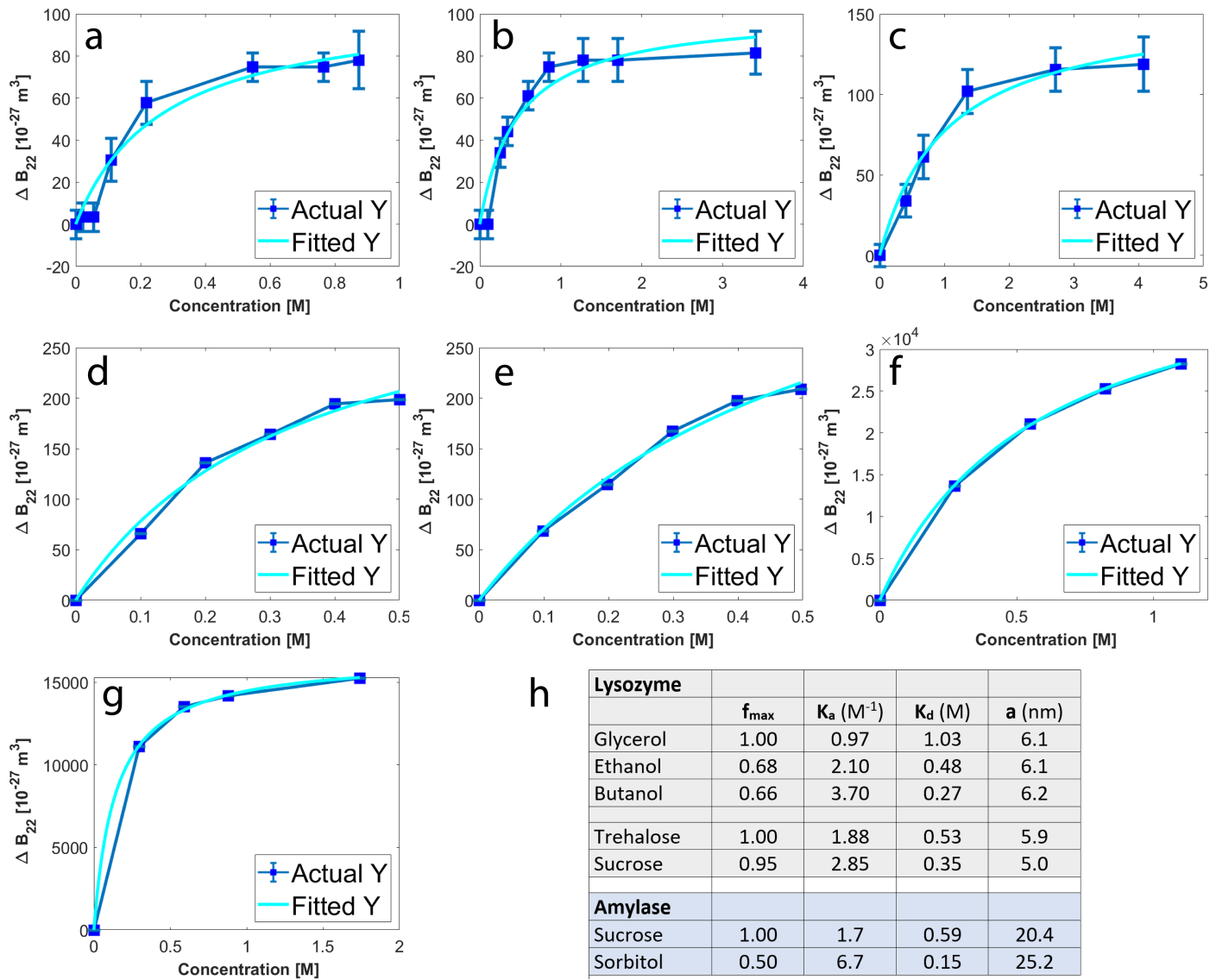
Extended Data Fig. 1 | Fitting of the B_{22} values from SE-AUC experiments with Eq. (1). Fitting was done to obtain the binding constant K_a between different amino acids and lysozyme and a value that represents maximum B_{22} . a) proline b) serine c) glycine and d) alanine. The dark blue dots represent

experimental means. The error bars are the experimental standard deviations obtained from 3 repetitions, and the light blue solid lines are the best fit. Table in e) contains results from the best fits. All the fits have the adjusted R^2 value no less than 0.96.

Article

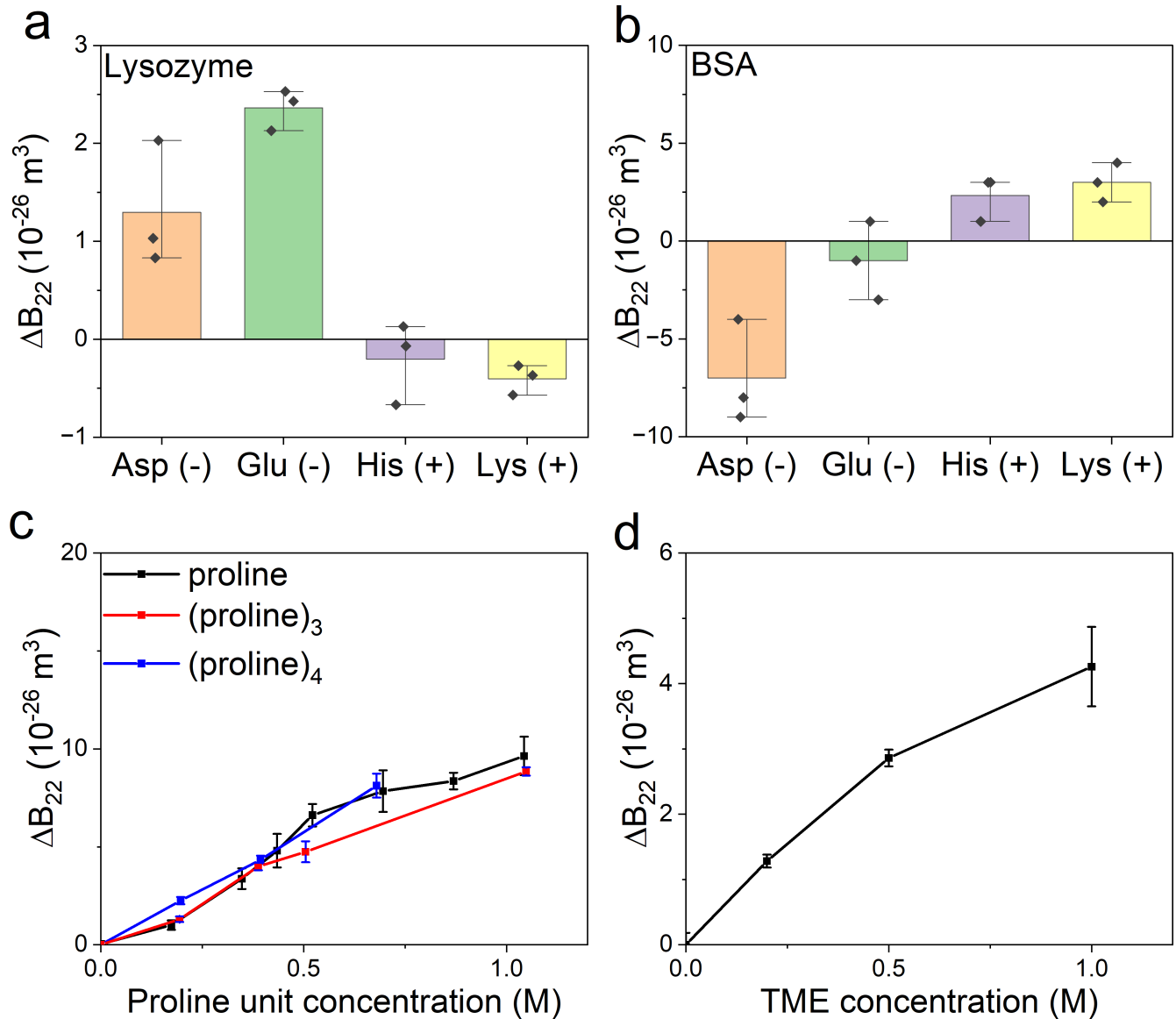


Extended Data Fig. 2 | Fitting of the B_{22} values from SE-AUC experiments with Eq. (1) to obtain binding constant K_a of proline on BSA. The equilibrium dissociation constant K_D is the reciprocal of K_a . Solid line plot is the experimental data, while the dash plot depicts the best fit.



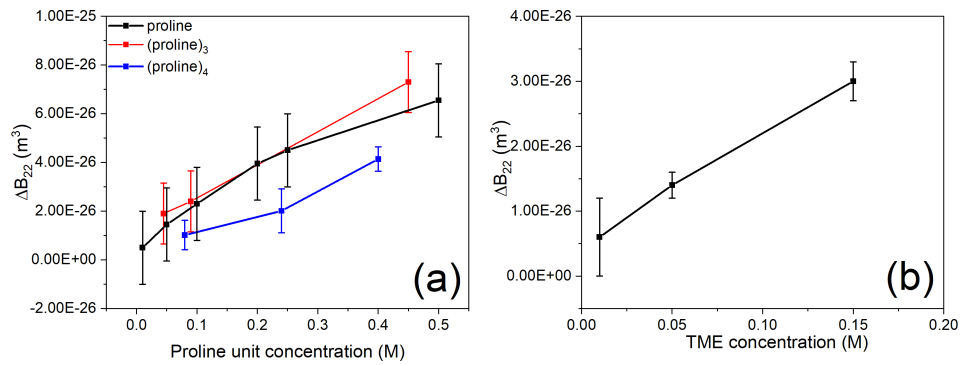
Extended Data Fig. 3 | Fitting of ΔB_{22} data reproduced from the literature. (a,b,c) effect of butanol, ethanol, and glycerol on lysozyme (W. Liu, D. Bratko, J. M. Prausnitz, H. W. Blanch, Biophys. Chem. 2004, 107, 289). Measurement conditions: 0.05 M NaCl, pH 7, and 25 °C. The second virial coefficients were measured by static light scattering methods. (d,e) effect of sucrose and trehalose on lysozyme. Condition: 0.1 M acetate, pH 4.5, 5% (w/v) NaCl. B_{22} was measured by SIC. Data reproduced from J.J. Valente, K.S. Verma, M.C. Manning, W. William Wilson, C.S. Henry, Biophys. J. 2005, 89, 4211. (f,g). Effect of sorbitol and sucrose on amylase. B_{22} was measured by SIC.

Data reproduced from J.J. Valente, B.G. Fryksdale, D.A. Dale, A.L. Gaertner, C.S. Henry, Anal. Biochem. 2006, 357, 35. The dark blue dots represent experimental means. The error bars are the experimental standard deviations, and the light blue solid lines are the best fit. Table in h) contains results from the best fits. Note that the set of data for the effect of sucrose and trehalose on lysozyme, the plateau of ΔB_{22} is missing. Similarly, it is the case for sorbitol and sucrose on amylase. Nevertheless, our model fits well, and the values of a found are less than 10% deviation from each other.

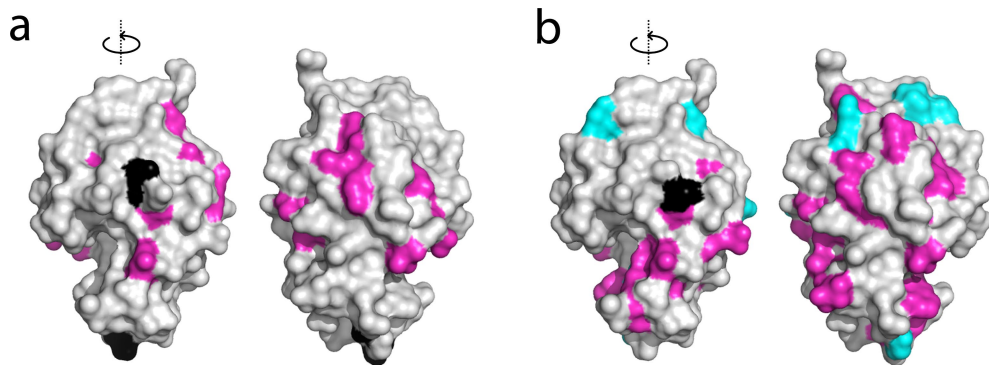


Extended Data Fig. 4 | Change of the second virial coefficient B_{22} (ΔB_{22}) by charged amino acids, poly-amino acids and the small molecule TME.
By applying SE-AUC we quantify the effect of two positively (histidine and lysine) and two negatively (aspartic acid and glutamic acid) charged amino

acids on the positively charged lysozyme (a) and on the negatively charged BSA (b) self-interaction at neutral pH. By applying SE-AUC we quantify the self-interaction of lysozyme in presence of poly-proline peptides (tri-proline ($\text{proline})_3$ and tetra-proline ($\text{proline})_4$) in comparison to proline (c) and of TME (d).

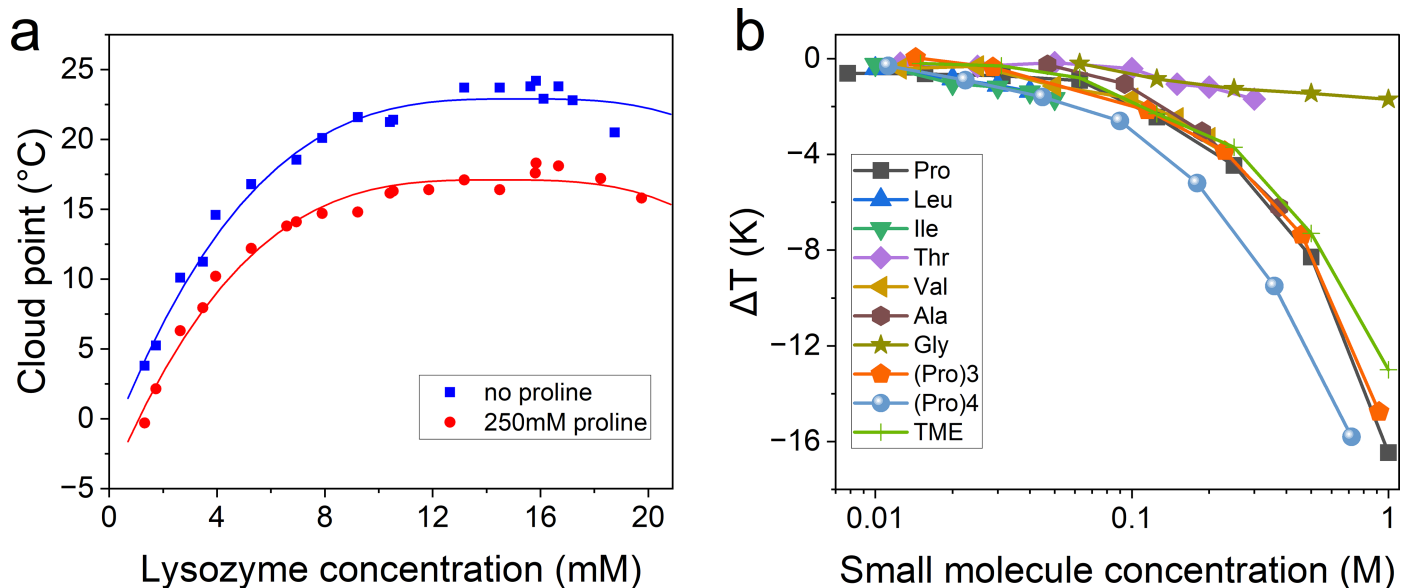


Extended Data Fig. 5 | Quantification of the self-interaction of lysozyme. This is done in presence of increasing concentration of poly-proline ($(\text{proline})_3$) and tetra-proline ($(\text{proline})_4$) in comparison to proline (a) and of TME (b).



Extended Data Fig. 6 | Amino acid adsorption “hot spots” on the surface of lysozyme. (a) by MD simulations (ff19SB protein, OPC water, simulation time 100ns, 5 replicas) and (b) by HSQC NMR. Protein residues that bind proline are colored in magenta, those that bind glycine in cyan, and those that bind both in black. In the MD analysis, a residue was taken to be an adsorption hot spot if the excess average binding number $\langle N_{AA,i}^* \rangle > 1$ at a bulk amino acid concentration of 1 M (i.e., on average, more than one amino acid lies within 5 Å of the residue). For HSQC NMR, what defined a hot spot was measurable non-linear chemical shift perturbation upon amino acid addition. The two maps do not coincide

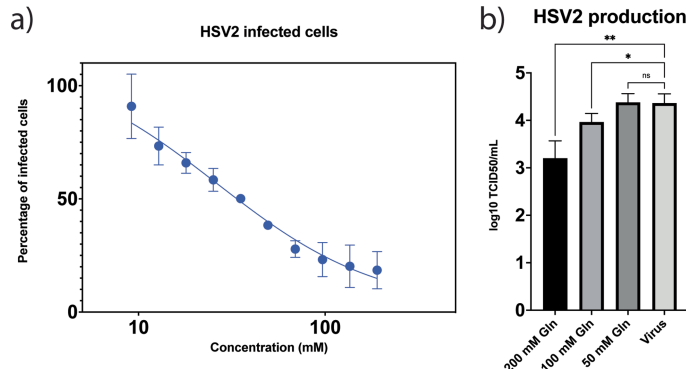
perfectly, likely because the sampling of adsorption-desorption events is inherently limited in the timescale of the MD simulations. Starting from a single crystal structure confines the ensemble of accessible protein conformations, so high-affinity adsorption sites that require a rare conformational opening may remain unsampled. Furthermore, HSQC NMR cannot resolve every backbone amide, leaving some adsorption sites invisible to the experiment, and some chemical shift perturbations may be caused by changes in hydration or conformation rather than direct amino acid contact.



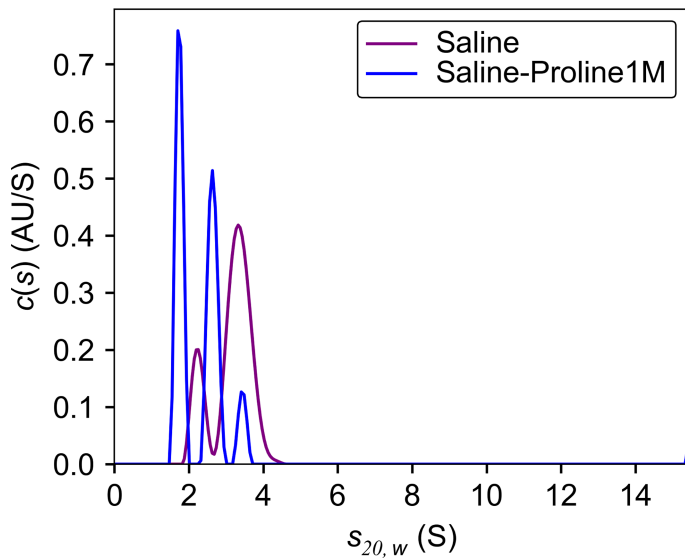
Extended Data Fig. 7 | Cloud point measurements of lysozyme. (a) parallel comparison of cloud point temperature of lysozyme in various concentration in phosphate buffer PBS 1× with added 0.5 M NaCl, and in phosphate buffer PBS 1× with added 0.5 M NaCl supplemented with 250 mM proline; (b) changes of cloud point temperature of lysozyme in PBS 1× with added 0.5 M NaCl with addition of different amino acids at varied concentrations, except for glycine and alanine where the buffer was PBS 1× with added 0.25 M NaCl for glycine, and phosphate buffer 50 mM for alanine. We fit our experimental data shown in a. We found that the critical temperature T_{cr} and the critical concentration C_{cr} to

be 22.9 °C and 15.3 mM in phosphate buffer PBS 1× with added 0.5 M NaCl, while they become 17.1 °C and 14.6 mM, respectively, upon the addition of 250 mM proline. The strength of stabilization depends on the proline concentration. This is shown in (b) where the ΔT for the phase line at lysozyme concentration of 7.0 mM is plotted against proline and many other AAs concentrations. This plot resembles the ΔB_{22} plot shown in Fig. 2b. The cloud point measurements confirm that AAs lead to measurable changes in ΔT at concentrations as low as 4.2 mM and at a protein to AA stoichiometric ratio as low as 1:0.5 (Fig. S5).

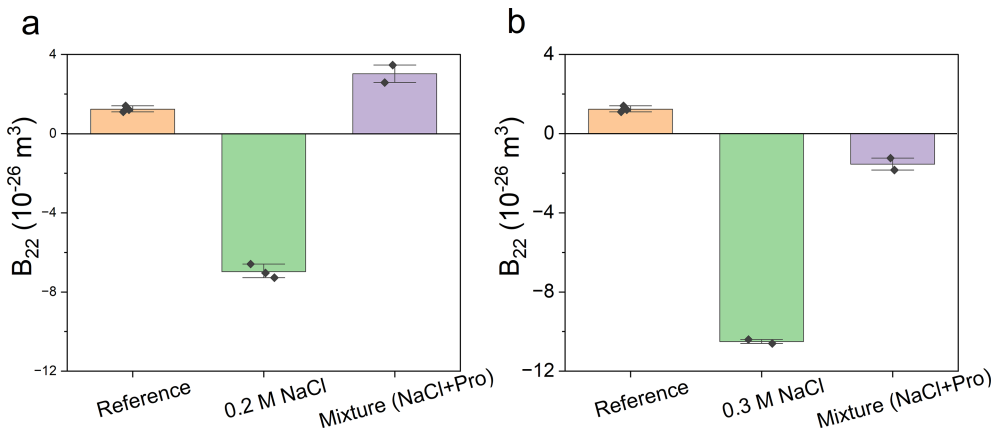
Article



Extended Data Fig. 8 | Effect of AA glutamine to reduce the replication of herpes simplex virus 2 (HSV-2) in Vero cells. (a) plot of the percentage of infected cells at a fixed MOI (multiplicity of infection) but at varying glutamine concentration. Clearly glutamine reduces the ability of HSV-2 to replication. Serial dilutions of glutamine were performed with a step of 1.4 then HSV2 MS strain (ATCC, VR-540) was added to obtain a final MOI of 0.1. Vero cells were infected with the different solutions and the infected cells were counted at 18 h post-infection by immunofluorescence. b) Bar plot of the TCID₅₀ (tissue culture infected dose) of Vero cells incubated 2 h with different concentrations of glutamine then infected with HSV2 MS strain (ATCC, VR-540). The supernatants were collected at 24 h post-infection and titrated by TCID₅₀ assay.



Extended Data Fig. 9 | Sedimentation velocity AUC to investigate the effect of proline on aggregate states of insulin in saline. The addition of 1 M proline (blue) to saline (violet) reduces the concentration of typical hexameric aggregates while increase substantially the aggregates of smaller aggregates including dimers. The first peak on left indicates the population of dimers; the last peak on right indicates the position of hexamers.



Extended Data Fig. 10 | Second virial coefficient B_{22} for the lysozyme-lysozyme interaction. B_{22} variation shows the opposite effect of proline to the known effect of a common salt such as sodium chloride. (a) lysozyme solution (reference), after the addition of NaCl (0.2 M) and the mixture (0.2 M NaCl + 1.0 M proline) and (b) lysozyme solution (reference), after the addition of NaCl (0.3 M) and the mixture (0.3 M NaCl + 1.0 M proline). The B_{22} for a lysozyme solution in 50 mM phosphate buffer (pH 7) was measured with AUC to be $+1.2 \times 10^{-26} \text{ m}^3$. The addition of 0.3 M of NaCl brings it to $-10.5 \times 10^{-26} \text{ m}^3$, as

expected salt lowers the B_{22} leading to net attractive interactions ($B_{22} < 0$). The further addition of 1.0 M proline to this solution brings back the B_{22} to the value of $-1.5 \times 10^{-26} \text{ m}^3$ showing that proline can indeed counter the effect of salt. In the case of the addition of 0.2 M NaCl the B_{22} becomes $-7.0 \times 10^{-26} \text{ m}^3$, now the addition of 1 M proline brings B_{22} not only back to being positive but also to a value larger than the starting one ($+3.0 \times 10^{-26} \text{ m}^3$), indicating that the effect of proline exceeds that of NaCl at this concentration.

Reporting Summary

Nature Portfolio wishes to improve the reproducibility of the work that we publish. This form provides structure for consistency and transparency in reporting. For further information on Nature Portfolio policies, see our [Editorial Policies](#) and the [Editorial Policy Checklist](#).

Statistics

For all statistical analyses, confirm that the following items are present in the figure legend, table legend, main text, or Methods section.

- | | |
|-----|-----------|
| n/a | Confirmed |
|-----|-----------|
- The exact sample size (n) for each experimental group/condition, given as a discrete number and unit of measurement
 - A statement on whether measurements were taken from distinct samples or whether the same sample was measured repeatedly
 - The statistical test(s) used AND whether they are one- or two-sided
Only common tests should be described solely by name; describe more complex techniques in the Methods section.
 - A description of all covariates tested
 - A description of any assumptions or corrections, such as tests of normality and adjustment for multiple comparisons
 - A full description of the statistical parameters including central tendency (e.g. means) or other basic estimates (e.g. regression coefficient) AND variation (e.g. standard deviation) or associated estimates of uncertainty (e.g. confidence intervals)
 - For null hypothesis testing, the test statistic (e.g. F , t , r) with confidence intervals, effect sizes, degrees of freedom and P value noted
Give P values as exact values whenever suitable.
 - For Bayesian analysis, information on the choice of priors and Markov chain Monte Carlo settings
 - For hierarchical and complex designs, identification of the appropriate level for tests and full reporting of outcomes
 - Estimates of effect sizes (e.g. Cohen's d , Pearson's r), indicating how they were calculated

Our web collection on [statistics for biologists](#) contains articles on many of the points above.

Software and code

Policy information about [availability of computer code](#)

Data collection No special code needed

Data analysis Data visualization and analysis by Prism, OriginPro, MS Excel, Imaris, Inspect3D

For manuscripts utilizing custom algorithms or software that are central to the research but not yet described in published literature, software must be made available to editors and reviewers. We strongly encourage code deposition in a community repository (e.g. GitHub). See the Nature Portfolio [guidelines for submitting code & software](#) for further information.

Data

Policy information about [availability of data](#)

All manuscripts must include a [data availability statement](#). This statement should provide the following information, where applicable:

- Accession codes, unique identifiers, or web links for publicly available datasets
- A description of any restrictions on data availability
- For clinical datasets or third party data, please ensure that the statement adheres to our [policy](#)

Data is available upon request to the authors. All raw data will be uploaded to a repository.

Research involving human participants, their data, or biological material

Policy information about studies with [human participants or human data](#). See also policy information about [sex, gender \(identity/presentation\), and sexual orientation](#) and [race, ethnicity and racism](#).

Reporting on sex and gender	<input type="checkbox"/> Not applicable
Reporting on race, ethnicity, or other socially relevant groupings	<input type="checkbox"/> Not applicable
Population characteristics	<input type="checkbox"/> Not applicable
Recruitment	<input type="checkbox"/> Not applicable
Ethics oversight	<input type="checkbox"/> Not applicable

Note that full information on the approval of the study protocol must also be provided in the manuscript.

Field-specific reporting

Please select the one below that is the best fit for your research. If you are not sure, read the appropriate sections before making your selection.

Life sciences Behavioural & social sciences Ecological, evolutionary & environmental sciences

For a reference copy of the document with all sections, see nature.com/documents/nr-reporting-summary-flat.pdf

Life sciences study design

All studies must disclose on these points even when the disclosure is negative.

Sample size	HSV experiment: Not applicable ; Stress granule experiment: Not applicable ; Animal study: Based on previous data, we need at least 6 mice per group to achieve 80% statistical power.
Data exclusions	HSV experiment: No data were excluded ; Stress granules experiment: No data were excluded ; Animal study: No data were excluded from the analyses.
Replication	HSV experiment: Glutamine dose response : 1 session in triplicate as the dose response protocol optimized in the lab demonstrated high reproducibility for the other compounds tested across different sessions. Viral production : 2 sessions, each one in triplicate. Multiple test comparisons using Dunnett and assuming a normal distribution and an equal standard deviation. Statistic test performed with GraphPad Prism 10.3.1 ; Stress granule experiment: More than 100 cells were analyzed in one single session ; Animal study: All attempts at replication were successful.
Randomization	HSV experiment: No relevant for these tests for a in vitro study to analyse the effect of one parameter ; Stress granule experiment: not applicable ; Animal study: The mice were randomly allocated into two groups.
Blinding	HSV experiment: No relevant for these tests for an in vitro study to analyse the effect of one parameter ; Stress granule experiment: not applicable ; Animal study: The in vivo experiments were conducted and data were analysed by two operators in a single blinded fashion.

Reporting for specific materials, systems and methods

We require information from authors about some types of materials, experimental systems and methods used in many studies. Here, indicate whether each material, system or method listed is relevant to your study. If you are not sure if a list item applies to your research, read the appropriate section before selecting a response.

Materials & experimental systems		Methods	
n/a	Involved in the study	n/a	Involved in the study
<input checked="" type="checkbox"/>	Antibodies	<input checked="" type="checkbox"/>	ChIP-seq
<input type="checkbox"/>	Eukaryotic cell lines	<input checked="" type="checkbox"/>	Flow cytometry
<input checked="" type="checkbox"/>	Palaeontology and archaeology	<input checked="" type="checkbox"/>	MRI-based neuroimaging
<input type="checkbox"/>	Animals and other organisms		
<input checked="" type="checkbox"/>	Clinical data		
<input checked="" type="checkbox"/>	Dual use research of concern		
<input checked="" type="checkbox"/>	Plants		

Eukaryotic cell lines

Policy information about [cell lines and Sex and Gender in Research](#)

Cell line source(s)	Vero cells, atcc ccl-81 HeLa cells (CCL-2™), ATCC.
Authentication	None of the cell lines were authenticated.
Mycoplasma contamination	Vero cells were tested negative for mycoplasma contamination (by PCR). For HeLa cells, we do a regular mycoplasma test in our cell lab and it is a negative result.
Commonly misidentified lines (See ICLAC register)	<i>Name any commonly misidentified cell lines used in the study and provide a rationale for their use.</i>

Animals and other research organisms

Policy information about [studies involving animals; ARRIVE guidelines](#) recommended for reporting animal research, and [Sex and Gender in Research](#)

Laboratory animals	C57BL/6 mice aged from 7 to 8 weeks were used in the study.
Wild animals	The study did not involve wild animals.
Reporting on sex	Male mice were used.
Field-collected samples	The study did not involve samples collected from the field.
Ethics oversight	All animal procedures were performed in compliance with protocols approved by the Animal Care and Use Committee of the Southern University of Science and Technology (Resolution number: SUSTech-JY202407031).

Note that full information on the approval of the study protocol must also be provided in the manuscript.

Plants

Seed stocks	Not applicable
Novel plant genotypes	Not applicable
Authentication	Not applicable